InFluence: An Open-Source Python Package to Model Images Captured with Direct Electron Detectors

Gearóid Liam Mangan, Grigore Moldovan, Andrew Stewart

Microscopy and Microanalysis, 2023, **29**, 1380–1401
https://doi.org/10.1093/micmic/ozad064
Advance access publication 14 July 2023
Original Article

Microscopy AND Microanalysis

InFluence: An Open-Source Python Package to Model Images Captured with Direct Electron Detectors

Gearóid Liam Mangan[1,2], **Grigore Moldovan**[3], **and Andrew Stewart**[2,*]

[1]*Physics Department, Faculty of Science and Engineering, University of Limerick, Limerick V94 T9PX, Ireland*
[2]*Department of Chemistry, University College London, 20 Gordon Street, London WC1H 0AJ, UK*
[3]*Point Electronic Gmbh, Erich-Neuss-Weg 15, Halle (Saale) D-06120, Germany*

***Corresponding author:** Andrew Stewart, E-mail: Andy.Stewart@ucl.ac.uk

Abstract

The high detection efficiencies of direct electron detectors facilitate the routine collection of low fluence electron micrographs and diffraction patterns. Low dose and low fluence electron microscopy experiments are the only practical way to acquire useful data from beam sensitive pharmaceutical and biological materials. Appropriate modeling of low fluence images acquired using direct electron detectors is, therefore, paramount for quantitative analysis of the experimental images. We have developed a new open-source Python package to accurately model any single layer direct electron detector for low and high fluence imaging conditions, including a means to validate against experimental data through computation of modulation transfer function and detective quantum efficiency.

Key words: detective quantum efficiency, direct detectors, electron microscopy, low fluence, medipix3, modulation transfer function, Monte Carlo methods, open-source

Introduction

Electron microscopes have proven to be a powerful tool for investigating the internal symmetry and morphologies of nano-sized matter. In the last few decades, interest has turned to innovating low dose and low fluence conventional electron microscopy (EM) and cryo-EM; methods that are employed to impede the structural changes associated with high beam fluences or doses (Carlson & Evans, 2012; Fujiyoshi, 2013; Egerton, 2019; Chen et al., 2020) (see Appendix for a discussion on terminology of dose, flux and fluence). An unfortunate ramification of using low fluences is reduced signal-to-noise ratios (SNRs) in the electron micrographs, complicating image interpretation, and measurement of structural features. Under low fluence conditions, high-angle diffraction peaks can be below detection limits because the scattering cross section decreases as a function of scattering angle. Modern direct detectors are one of the many innovations used to combat the challenges of low dose and low fluence EM experiments (Chen et al., 2020). In particular, these new detectors are more efficient at detecting incident electrons for a number of reasons. Firstly, they directly detect incident particles by measuring the charges generated in each pixel by the incident radiation. Direct detection avoids some of the signal-loss mechanisms that are associated with indirect detection (Fernandez-Perez et al., 2021). Secondly, they can detect single electron events by choosing an appropriate detection threshold, thereby eliminating readout noise (Paterson et al., 2020). Higher efficiencies lower the information dose and fluence limits, below which useful or desired information cannot be obtained from the image or pattern.

Direct electron detectors can be distinguished into two groups: hybrid pixel detectors (HPDs), such as the Medipix detectors (Ballabriga et al., 2018), and monolithic active pixel sensors (MAPS), such as the Falcon 3 and 4 (Guo et al., 2020) and the Gatan K2 (Booth, 2012) and K3 (Feathers et al., 2021; Sun et al., 2021). Generally speaking, MAPS detectors typically have arrays of pixels that are smaller and more numerous than HPD arrays but are limited by a comparatively poor dynamic range when operating in counting mode. Counting mode is an operating mode in which the frame rate increases to better count individual electron impingements. Accurate detection of individual electron impingements is subject to frame rate and coincidence loss imposed by significant readout speeds. By extension, coincidence loss reduces the dynamic range of the detector. Counting mode differs from the conventional linear mode in which energy deposition over the *total* exposure time is integrated, which makes it impossible to know the exact number of electrons impinging on a pixel during that exposure time. The differences of MAPS detectors and HPDs ensure that each one has distinct applications. For example, the smaller pixels and large field of view of MAPS detectors position them as particularly well suited for single particle cryo-EM imaging (Li et al., 2013; Fan et al., 2019; Nakane et al., 2020), while their relatively poor dynamic range in counting mode limits their usefulness in high fluence diffraction experiments because coincidence loss results in inaccurate intensity measurements of low-resolution diffraction peaks. Note, however, under low fluence conditions, MAPS detectors are desirable in diffraction experiments as counting mode is advantageous in accurately recording weak, high-resolution diffraction peaks. Conversely, HPDs are ideal for

Received: April 25, 2022. **Revised:** April 26, 2023. **Accepted:** May 3, 2023

high fluence diffraction experiments on crystalline matter if the unit cells are sufficiently small to ensure that resolution of diffraction peaks is uncompromised by measurement with their small arrays of large pixels (Clabbers et al., 2017).

In general, direct detectors are capable of recording high intensities and also of reading out at high speeds to minimize the exposure of the specimen to the beam (Paterson et al., 2020). Both of these qualities make them highly suited for advanced electron diffraction experiments, for example, four-dimensional STEM (4DSTEM) experiments (Ophus, 2019) and three-dimensional electron diffraction (3DED) experiments (Gemmi et al., 2019). 4DSTEM involves the acquisition of two-dimensional (2D) diffraction patterns from a 2D scan grid; such data sets are valuable because they can be processed in many ways to give different microstructural information. For example, since the intensities of the collected patterns are dependent on the area underneath the illuminating probe, the 4DSTEM data set can be processed to create a map of crystalline orientations or phases. Simultaneously, the 4DSTEM data set can also be used for phase retrieval by application of ptychographic algorithms (Rodenburg, 2008; Ophus, 2019). 3DED techniques involve the collection of diffraction patterns as the crystal is rotated or as the beam is deflected; the set of patterns is a sample of the reciprocal lattice that can be related to the direct lattice with sophisticated reconstruction algorithms (Gemmi et al., 2019; Gruene & Mugnaioli, 2021).

With the wide application of direct detectors in the collection of higher quality data, it is pertinent that image simulations are adapted to ensure an appropriate comparison to results from experiments in which these detectors are employed. To elaborate, conventionally, the image contrast in experimental TEM data is often three to five times less than that predicted by theoretical models for both crystalline and amorphous materials over a wide range of spatial frequencies. Researchers have made efforts to account for the so-called Stobbs factor in experiment by considering a variety of electron scattering models and how they modify the coherent Bragg peak intensities and the background (Howie, 2004). The considerable improvements in these models and their implementations have not been enough to close the gap between experiment and simulation. However, Thust (2009) showed that the additional inclusion of empirical frequency-transfer properties of the detector, through the modulation transfer function (MTF), in simulations led to near perfect consistency between simulation and experiment. Moreover, Jia et al. (2013, 2014) show quantitative fits of simulations to experiments by inclusion of the measured MTF. It must be noted that images simulated using empirical MTF data are limited to comparison with experimental images taken under similar conditions as the MTF data.

In the subsequent sections, we elaborate on the limitations of applying empirical MTF data to simulation and discuss InFluence, a new software package in Python that utilizes the Monte Carlo single scattering model outlined in Joy (1995) to simulate physical experiments in which S/TEM images of arbitrary exposure conditions are obtained from any single layer gapless direct detector operating in single pixel mode (SPM) (the details of this operating mode are discussed later in the Medipix3 Specifications section). The Monte Carlo single scattering model accurately captures the propagation of the electron in the sensor layer as it deposits energy for charge production. Calculation of each electron trajectory is handled separately, and by extension, imaging at low fluences can be accurately simulated. InFluence does not model the geometry of the specimen; InFluence is applied to an image simulated by a multislice (for an in depth account of the formulation of the multislice method, see Earl J. Kirkland's book Advanced Computing in Electron Microscopy, specifically chapter 6 (Kirkland, 2020)) package, such as abTEM (Madsen & Susi, 2021) or Dr. Probe (Barthel, 2018), completing the simulation workflow by adding the effects of measurement by a simulated detector. This is different to the usage of a software such as CASINO (Drouin et al., 2007), which can model samples and detector geometries with vertical and horizontal planes, because CASINO cannot be applied to an image produced by a multislice package in the same way.

InFluence is open and freely available to use, fitting into the growing ecosystem of open free simulation and data processing packages for S/TEM, which includes abTEM, Pyxem (Cautaerts et al., 2021), Atomap (Nord et al., 2017), HyperSpy (de la Pena et al., 2021), TEMUL Toolkit (O'Connell et al., 2022), Prismatic (Ophus, 2017; Pryor et al., 2017; Rangel DaCosta et al., 2021), LiberTEM (Clausen et al., 2021), and AtomAI (Ziatdinov et al., 2022).

Theory

Medipix3 Specifications

We chose to model the Medipix3 HPD because the technology underpinning the detector is well documented; however, parameters within the software can be adjusted by users to simulate other HPDs. This model of the Medipix3 is composed of a 1-μm-thick aluminum film that sits on top of a 300-μm-thick silicon layer that is bump bonded to an application-specific integrated circuit (ASIC), which is the pixel array and readout circuitry. The pixels are modeled as squares with a side of length 55 μm. There are 256×256 pixels on a detector array (Ballabriga et al., 2011; Paterson et al., 2020). For the purposes of the simulation, the origin of a pixel is at its center. A defined origin is important because the Monte Carlo simulations, discussed elsewhere, are calculated for each pixel in the detector array and the origin is a reference point used to check whether the electron has scattered into a neighboring pixel. The choice of origin for each pixel is arbitrary but needs to be consistent.

The Medipix3 uses hybrid particle counting technology, schematic shown in Figure 1: by coating the silicon with an aluminum film, it is possible to apply a biasing voltage across the detector. As the electrons scatter in the detector, they deposit energy that is used in electron–hole pair production. For silicon, the energy per pair is assumed to be 3.6 eV. The electric field generated by the applied bias causes the holes to move toward the ASIC and the electrons to move toward the aluminum film. The holes induce a signal at the analog part of the ASIC pixel. Additionally, the aluminum film also serves as a shield against visible light and soft X-rays.

In SPM, an incident electron is detected in a pixel if the signal measured in that pixel exceeds a chosen threshold, T_{counting}, (Paterson et al., 2020). Electrons have sufficient energy to travel laterally into neighboring pixels and deposit energy to generate charges in those pixels, leading to the possibility that the ASIC counts the incident electron more than once in the incident pixel and/or neighboring pixels if the threshold value has been set too low. It is also possible that the ASIC *does not* count the incident electron at all if

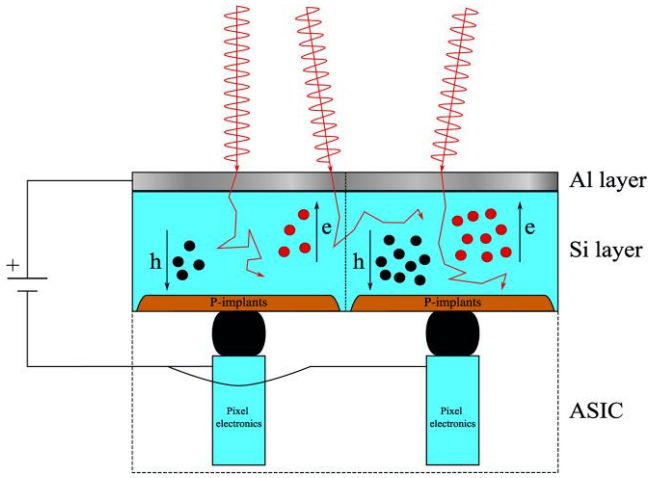

Fig. 1. Simplified schematic of the hybrid particle counting technology. The aluminum layer sits on top of the silicon substrate enabling the application of a biasing voltage between the particle counting pixel electronics contained in the ASIC and the aluminum layer. The particle is incident on the aluminum layer and then gets scattered in the aluminum and silicon substrates. After each scattering event, the incident particle loses energy, which is used in electron–hole pair production. The generated electrons (red circles) flow towards the aluminum layer at the positive side of the bias and the holes (black circles) flow towards the pixel electronics at the negative side of the bias. Note that one of the particles is incident near the pixel boundary (dashed vertical line) and is subsequently scattered into the neighboring pixel; the electron–hole pairs it produces by energy deposition are counted by the neighboring pixel's electronics, which leads to image blurring.

the threshold value has been set too high. The ability to choose the counting threshold enables the user to maximize either the MTF or the DQE because the number of incident electrons counted and their lateral spread are directly related to the DQE and MTF (Mir et al., 2017; Paterson et al., 2020). On a final note with respect to thresholding, there is a lower limit to the choice a user can make for the threshold: it should be set above the chip's thermal electronic noise floor, which is just under 5 keV for the Medipix3 (Mir et al., 2017).

The electron loses energy in the aluminum film. The aluminum film can also be modeled as a structureless continuum (see the Assumptions of the Single Scattering Model section) and placed on top of the silicon layer in a Monte Carlo simulation. However, to reduce code complexity, we chose to approximate the *average* energy lost in the aluminum film by performing a separate calculation of the electron scattering in the aluminum film that is then incorporated into the overall calculations within our software InFluence. We subtract the average loss from the chosen initial electron energy of the incident beam. The implication of this is that we have removed the noise associated with the natural variance of the electron energy as a result of scattering within the aluminum layer. According to Equation (2), the mean free path decreases as a function of incident energy, implying that the average time an electron spends in the aluminum layer increases with decreasing incident energy. In addition, Equation (21) shows that low-energy electrons lose more energy per distance travelled. Collectively, this means that the energy lost to the aluminum layer becomes more significant as the incident energy of the electron decreases. In the case of 80- and 200-keV electrons, making this compromise introduces negligible error. Our simulations revealed that the average energy loss is ~1.1 keV in the aluminum layer for an 80-keV electron beam and ~0.8 keV for a 200-keV electron beam.

The ASIC takes a finite time to process each pulse induced by an incident electron. This leads to an underestimation of the signal if another electron induces a pulse during this processing time. The model presented in this paper assumes that no electrons are incident on a pixel during this processing time (Fröjdh et al., 2015). In fact, the model in this paper assumes that only one electron travels through the column and the detector until counting is completed. This is a valid assumption for low flux experiments. Consider the case in which the electrons are travelling through a TEM column of length d at speed v. Since an electron takes $\frac{d}{v}$ to travel through the column, there is a neglibilible chance of two electrons travelling through the column simultaneously if $F \times \frac{d}{v} \ll 1$, where F is the flux (e/Å^{2}s).

Single Scattering Model

Monte Carlo models can be used to simulate electron scattering in a material, where the material is continuous and structureless. Here, we offer a summarized version of the elastic single scattering models given in Joy (1995) and Lowney et al. (1994) for the convenience of the reader. We have not made changes to the models.

The single scattering model is a method used to generate a distribution of possible scattering trajectories for a particle incident on some materials. In the context of this paper, the particle in question is an electron. The experimental geometry follows a right-handed Cartesian coordinate system, with the positive z-axis pointing into the material, as shown in Figure 2.

The electron undergoes a scattering event and travels a distance s from point P_n to point P_{n+1}. The distance travelled is given by

$$s = -\lambda \log_e(\mathrm{RND}), \tag{1}$$

where λ is the mean free path of the incident electron and RND is a random number selected from a distribution with a range from 0.000001 to 0.999999. The mean free path is given by

$$\lambda = \frac{A}{N_A \rho \sigma_M}, \tag{2}$$

where N_A is Avogadro's number, ρ is the density of the target (g/cm^3), and A is the atomic weight of the target (g/mole). σ_M (cm^2) is the Mott scattering cross section parametrized by Browning (1991) and is written as

$$\sigma_M = 4.71 \times 10^{-18} \frac{(Z^{1.33} + 0.032Z^2)}{(E + 0.0155Z^{1.33}E^{0.5})} \times \frac{1}{(1 - 0.02Z^{0.5}e^{-u^2})}, \tag{3}$$

where E is the electron energy (keV) and Z is the atomic number and u defined as

$$u = \log_{10}(8EZ^{-1.33}). \tag{4}$$

The azimuthal scattering angle ψ of the electron can be any number within the range 0° and 360° and is defined by

$$\psi = 2\pi \mathrm{RND}_\psi. \tag{5}$$

The polar scattering angle ϕ of the electron can be any number within the range 0° and 180° and is defined by the relationship

$$\phi = \arccos\left(1 - \frac{2\xi \mathrm{RND}_\phi^2}{(1 + \alpha - \mathrm{RND}_\phi)}\right), \tag{6}$$

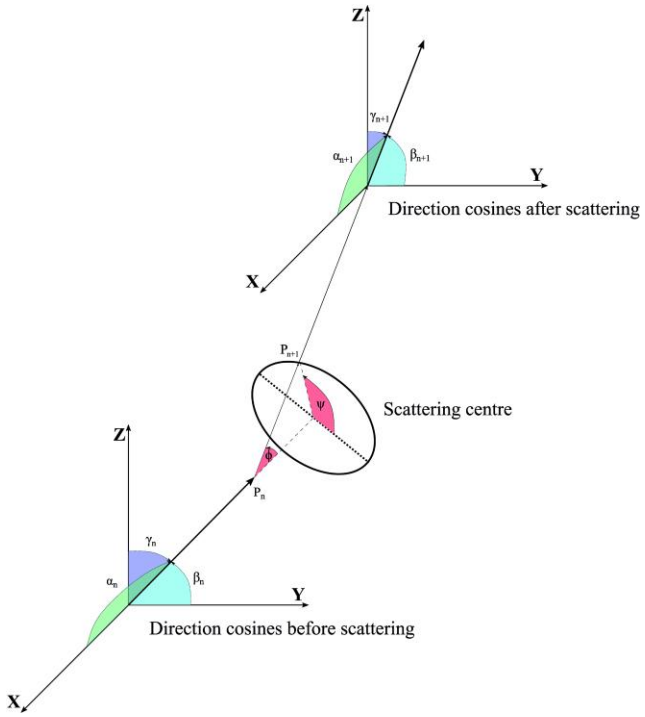

Fig. 2. Coordinate system used in this Monte Carlo single scattering simulation. α, β, and γ are the angles between the position vector of the scattered electron and the x-, y-, and z-axes. ϕ and ψ are the polar and azimuthal scattering angles. P_{n+1} is the position of the electron after a scattering event occurs at its previous position P_n.

where ξ is a parameter that accounts for nuclear screening (Joy, 1995).

$$\xi = 0.0034\left(\frac{Z^{0.67}}{E}\right). \tag{7}$$

RND_ψ and RND_ϕ are random numbers chosen from a uniform distribution with values in the range 0 and 1. The Mott scattering cross section more accurately describes the elastic scattering of the electron at low beam energies (<20 keV) and for nuclei with higher atomic numbers ($Z > 30$) (Czyżewski et al., 1990). The angular distribution for this Mott model is square and is approximated by modifying the Rutherford polar scattering angle (Joy, 1995).

In the model presented in this paper, the electron scattering begins after the electron has already penetrated the detector, meaning that the initial penetration depth z is determined using Equation (1). The x and y coordinates are randomly selected from a uniform distribution with a user-defined minimum and maximum: the minimum is −1 times the maximum. For the simulated Medipix3 model, the user should choose half the pixel (which is modeled as a square) side length as maximum since the origin of the simulation is at the center of the detector pixel. Hence, the following equations define the initial positions:

$$z = s, \tag{8}$$

$$x = d \times \mathrm{RND}_x, \tag{9}$$

$$y = d \times \mathrm{RND}_y, \tag{10}$$

where s is the scattering step length, d is the user-defined maximum, and RND_x and RND_y are random numbers chosen from a uniform distribution with values in the range −1 and 1. These equations can be easily adjusted to accommodate any arbitrary definition of the origin and pixel (or material) dimensions. For example, for a rectangular pixel, the d parameter would be changed to reflect the difference between the maximums in the x and y directions.

The position of the electron after a scattering event is calculated by

$$x_n = x_{n-1} + s \times c_a, \tag{11}$$

$$y_n = y_{n-1} + s \times c_b, \tag{12}$$

$$z_n = z_{n-1} + s \times c_c, \tag{13}$$

where x_{n-1}, y_{n-1}, and z_{n-1} are the components of the position vector along the x, y, and z axes, respectively, and c_a, c_b, and c_c are the direction cosines of the electron position vector after scattering has occurred. Illustrated in Figure 2, the new direction cosines are related to the old direction cosines c_x, c_y, and c_z through the polar, ϕ, and azimuthal, ψ, scattering angles:

$$c_a = \frac{1}{a_2}[a_1 c_y + c_x(a_3 c_z + a_2\cos(\phi))], \tag{14}$$

$$c_b = -\frac{1}{a_2}[a_1 c_x + c_y(a_3 c_z + a_2\cos(\phi))], \tag{15}$$

$$c_c = -a_2 a_3 + c_z\cos(\phi), \tag{16}$$

where

$$a_1 = \sin(\phi)\sin(\psi), \tag{17}$$

$$a_2 = (1 - c_z^2)^{0.5}, \tag{18}$$

$$a_3 = \sin(\phi)\cos(\psi). \tag{19}$$

The full derivation and further explanation of these equations can be found in Lowney et al. (1994); however, we make note of some important aspects of the equations and derivation: the sum of each old direction cosine squared must equal the sum of each new direction cosine squared, which must both equal to 1. Alternatively stated, the following equation must hold true:

$$c_x^2 + c_y^2 + c_z^2 = c_a^2 + c_b^2 + c_c^2 = 1. \tag{20}$$

The coordinate system is rotated after a scattering event occurs. For consistency and for Equation (20) to be satisfied, the new direction cosines representing the new position of the electron must be represented in the original coordinate system. This is achieved by two rotations, one about the x-axis and the other about the z-axis.

The electrons lose energy through their Coulomb interactions with the positive nuclei in the scattering material. The electrons also lose energy discretely due to inelastic scattering events. We can approximate the total electron energy change per distance travelled by the modified Bethe equation, which is more appropriate than the original form at lower beam energies, i.e., when the electron energy E (keV) is less than or equal to the mean ionization energy $E_{\mathrm{ionization}}$ (keV) (Joy, 1995):

$$\frac{dE}{ds} = -78{,}500\frac{Z}{AE}\log_e\left(\frac{1.166(E + 0.85E_{\mathrm{ionization}})}{E_{\mathrm{ionization}}}\right), \tag{21}$$

where A is the atomic weight (g/mole). J is measured experimentally for different materials (Berger et al., 1984) but can be estimated using the equation (National Research Council, 1964):

$$E_{\text{ionization}} = \left(9.76 \times Z + \frac{58.5}{Z^{0.19}}\right) \times 10^{-3}, Z \geq 13$$
$$E_{\text{ionization}} = 11.5Z, \; Z < 13. \quad (22)$$

With all the necessary equations defined, we now describe how an electron propagates through a material. The user defines the properties of the scattering material and the energy of the electron. The initial coordinates are calculated using Equations (8)–(10). The electron then scatters to a new position, whose coordinates are calculated using Equations (11)–(13). The energy that the electron loses is calculated using Equation (21). This process is repeated until the energy of the electron falls below a user-defined threshold at which point the electron is assumed to have insufficient energy to move through the material or if the electron exits the material by backscattering or by transmission. Our application of this model to image simulation is discussed later.

Assumptions of the Single Scattering Model

The spatial distribution of the electrons is dominantly determined by elastic collisions (Joy, 1995). Hence, discrete inelastic scattering events are not *directly* modeled; instead, the energy is continuously lost to the surrounding material. Furthermore, the model assumes that the energy losses in the simulated specimen are negligible compared to the total energy of the electron and the energy losses in the detector. The model assumes that energy lost to the detector is used for electron–hole pair generation and ignores other types of inelastic scattering processes. In general, neglect of these phenomena adds some uncertainty in the true noise of simulation. However, contributions from secondary electron generation, for instance, are minor and can be ignored for the purposes of contrast modulation.

The Medipix detectors (which are discussed in the Medipix3 Specifications section) are composed of crystalline matter; however, the single scattering model assumes that the detector is continuous and structureless. This assumption holds when the step length is larger than the crystal lattice parameters, because the step length defines which features or effects are resolved. In effect, phenomena that arise due to crystallinity, such as electron channeling and diffraction, are not considered. We expect the structureless model to be sufficient for this study as the most important outcome of the Monte Carlo simulation is determining the lateral spread of the electrons in the detector.

Methodologies

The following subsections describe our methods for generating the data. In summary, to simulate an image with a use-specified finite fluence and the contrast modulation due to the electron scattering within a detector, the user should first generate an image from an image simulation package, such as Dr. Probe (Barthel, 2018), MULTEM (Lobato & Van Dyck, 2015), Prismatic (Ophus, 2017), or abTEM (Madsen & Susi, 2021). The pixel intensities of the images simulated from these packages represent probabilities of an electron scattering to that pixel. The intensities are normalized such that their sum is one. This description extends to the slanted edge and flat-field images before simulating finite fluences; therefore, we denote all inputs to InFluence as normalized images. The first, and most simple, task of InFluence is to convert the normalized image to one with a user-specified finite fluence. The second, and final, task is to simulate electron scattering in a detector with user-defined properties.

The simulated detector is characterized by application of the slanted edge method and the relevant metrics: the MTF, the noise power spread (NPS), and the detective quantum efficiency (DQE). For a detailed description of these methods, see the Detector Characterization section in the appendices. The MTFs and NPSs were obtained with a JavaScript plugin for ImageJ (Schneider et al., 2012). DQEs are computed from the MTFs and NPSs according to Equation (27).

Simulations and analysis were performed on a computer with a Windows 10 operating system, an Intel Core i5 6600K central processing unit (CPU) overclocked to 4.2 GHz, 16 GB of random-access memory and an NVIDIA GeForce GTX 980 Ti graphics processing unit (GPU).

InFluence

InFluence is a software designed to simulate a modulated image of arbitrary electron fluence. To be clear, a modulated image is a simulated image that takes into account intensity modulation that arises from electron–detector interactions. InFluence will be available on GitHub in conjunction with this publication. The code is written in Python version 3.6.8 (van Rossum & Drake, 2009) and makes use of several highly optimized libraries, including NumPy (Oliphant, 2006), math, random, time (Van Rossum, 2018), SciPy (Virtanen et al., 2020), Numba (Lam et al., 2015), and Matplotlib (Hunter, 2007). We have not tested other versions of Python but expect that InFluence should be compatible with most, if not all, future versions with perhaps minor changes to the code. For the convenience of the user, the code is separated into four PY files: InFluence.py, plot_trajectories.py, common_functions.py, and params.py. InFluence.py uses the single scattering Monte Carlo model outlined in the Theory section to calculate the trajectories of the electrons in a HPD. The model is defined by a set of functions stored in the

Table 1. Runtimes of Standard InFluence for Several Simulation Conditions.

Number of Pixels	Number of Electrons	Energy (keV)	Time Taken (s)
256 × 256	500,000	200	259.43 ± 3.61
256 × 256	50,000	200	29.77 ± 0.15
10 × 10	500,000	200	199.07 ± 13.18
10 × 10	50,000	200	23.97 ± 3.33
256 × 256	500,000	80	144.35 ± 6.78
256 × 256	50,000	80	18.83 ± 1.42

Table 2. Runtimes of Alternative InFluence for Several Simulation Conditions.

Number of Pixels	Number of Electrons	Energy (keV)	Time Taken for Alternative InFluence (s)
256 × 256	500,000	200	111.25 ± 2.26
256 × 256	50,000	200	12.59 ± 1.47

The time taken to load the 2,000 sample distribution is 43.03 ± 2.90. The time taken for the alternative InFluence to modulate an image does not include the load time of the sample distribution.

Table 3. Runtimes of Standard and Alternative InFluence for Parallel Mode set to True.

	Number of Pixels	Number of Electrons	Energy (keV)	Time Taken for Standard InFluence (s)	Time Taken for Alternative InFluence (s)
First image	256×256	50,000	200	25.75 ± 1.50	17.54 ± 1.07
Subsequent images	256×256	50,000	200	8.92 ± 1.16	4.43 ± 1.15

The time taken to load the 2000 sample distribution is 43.03 ± 2.90. The time taken for the alternative InFluence to modulate an image does not include the load time of the sample distribution.

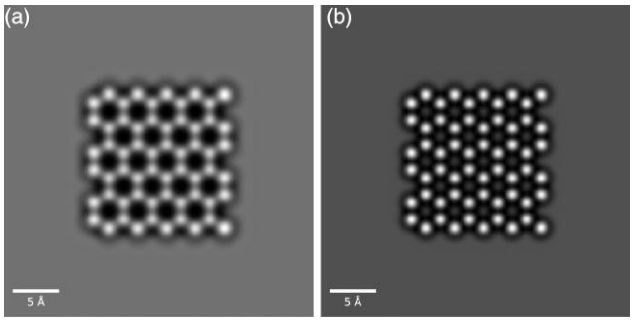

Fig. 3. Simulated (**a**) 80- and (**b**) 200-keV normalized TEM images of an MoS_2 lattice surrounded by vacuum.

common_functions.py file. Plot_trajectories.py enables the user to also visualize the lateral spread and penetration depth of the electrons. The experimental parameters for both InFluence.py and plot_trajectories.py can be adjusted in the params.py file. The code is not limited to the Medipix family; adjustment of the detector material properties enables simulation for any HPD with a single sensor layer and gapless pixels. These material properties are the atomic number, the atomic weight, the material density, the detector thickness, the energy threshold for electron–hole pair generation, and the pixel side length.

For simulating physical experiments, the input image to InFluence is the output from an image simulation software (ISS), such as abTEM, without any MTF file applied. In the

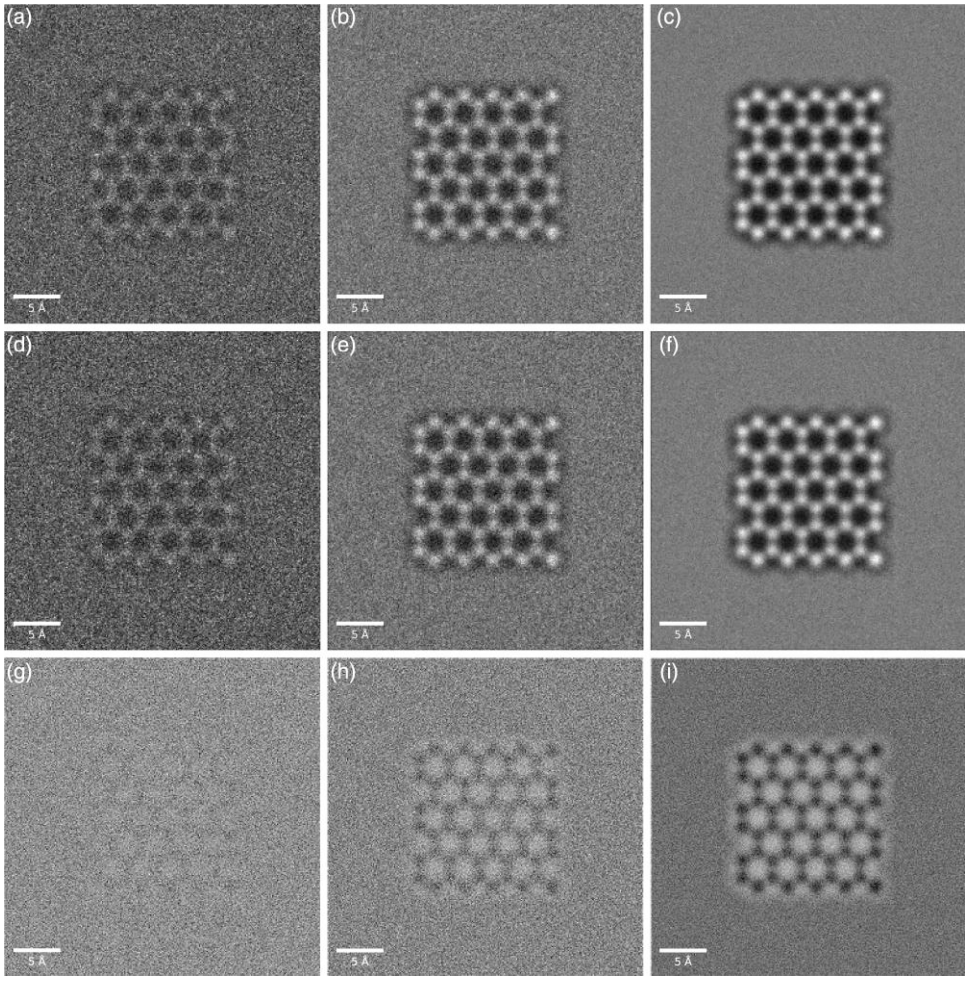

Fig. 4. Application of InFluence to unmodulated (**a**) low fluence (10 e/pixel), (**b**) medium fluence (100 e/pixel), and (**c**) high fluence (1,000 e/pixel) images of an MoS_2 lattice, resulting in the modulated (**d**) low fluence, (**e**) medium fluence, and (**f**) high fluence images. (**g**)–(**i**) are the different maps for low, medium, and high fluence simulations, calculated by subtracting the modulated images from the unmodulated images. The electrons are incident with an energy of 80 keV, and the energy of the electron–hole pairs are counted using a threshold of 32 keV.

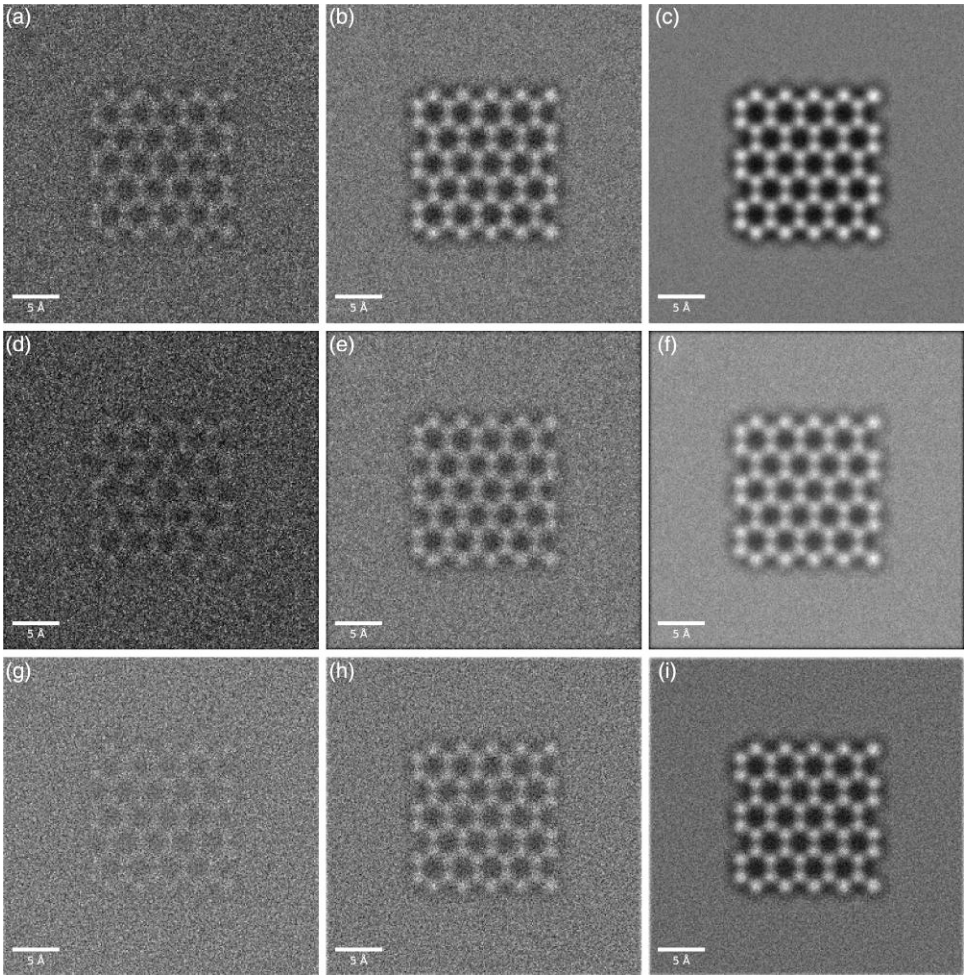

Fig. 5. Application of InFluence to unmodulated (**a**) low fluence (10 e/pixel), (**b**) medium fluence (100 e/pixel), and (**c**) high fluence (1,000 e/pixel) images of an MoS_2 lattice, resulting in the modulated (**d**) low fluence, (**e**) medium fluence, and (**f**) high fluence images. (**g**)–(**i**) are the difference maps for low, medium, and high fluence simulations, calculated by subtracting the modulated images from the unmodulated images. The electrons are incident with an energy of 200 keV, and the energy of the electron–hole pairs are counted using a threshold of 80 keV.

case of validating a direct detector, a flat-field noise image and slanted edge image are the appropriate inputs. In subsequent sections, we show results for 32-bit floating point square images stored as both NumPy and TIFF format, but InFluence could accept any rectangular image of any size and bit format with relatively trivial modifications to the file-opening function of InFluence. The normalized images are converted to finite fluence images using Poisson noise with Numpy.

To simulate how an ASIC detects electrons, InFluence processes the scattering of the electrons in each pixel separately, while counting the number of electron–hole pairs generated in a pixel by the incident electrons as they propagate through the pixel (and perhaps its neighbors); if the energy of the pairs in a single pixel exceeds the threshold, T_{counting}, defined in params.py, an electron is detected in that pixel. InFluence runs until the trajectories of every electron incident on every pixel are calculated. The results in Table 1 show that larger images do equate to significant increases in runtime as iterating over pixels is inefficient. Furthermore, the number of electrons and their energy also contribute significantly to the runtime.

In conjunction with the standard version of InFluence is a version that enables the user to load a precalculated distribution of possible electron trajectories from file instead of calculating the trajectory of each electron in real time. A larger number of samples ensure a higher confidence in the sample distribution but require greater overhead in the loading time of the distribution file. With this in mind, this alternative version of InFluence is faster when the load time is negligible when compared to the time it takes to assign a trajectory to each electron in the simulation. For example, comparing the results in Tables 1 and 2, it is clear that the standard version of InFluence is faster for 50,000 electrons, but slower for 500,000 when taking the time taken to load the sample distribution into account. That being said, the distribution only needs to be loaded a single time when executing InFluence, implying that modulating a set of images in a single run of InFluence can realize additional savings for computational time.

Furthermore, parallel mode with Numba can be enabled for the standard and alternative versions of InFluence. There are no drawbacks to enabling parallel computation for standard InFluence, whereas additional compilation time is needed for the alternative version of InFluence; however, comparison of the results in Tables 2 and 3 shows that this cost can be offset if several images are simulated with a single run of InFluence.

It must be noted that the results in Tables 1–3 are relevant only for the workstation described above and are subject to change depending on the exact computational power of the

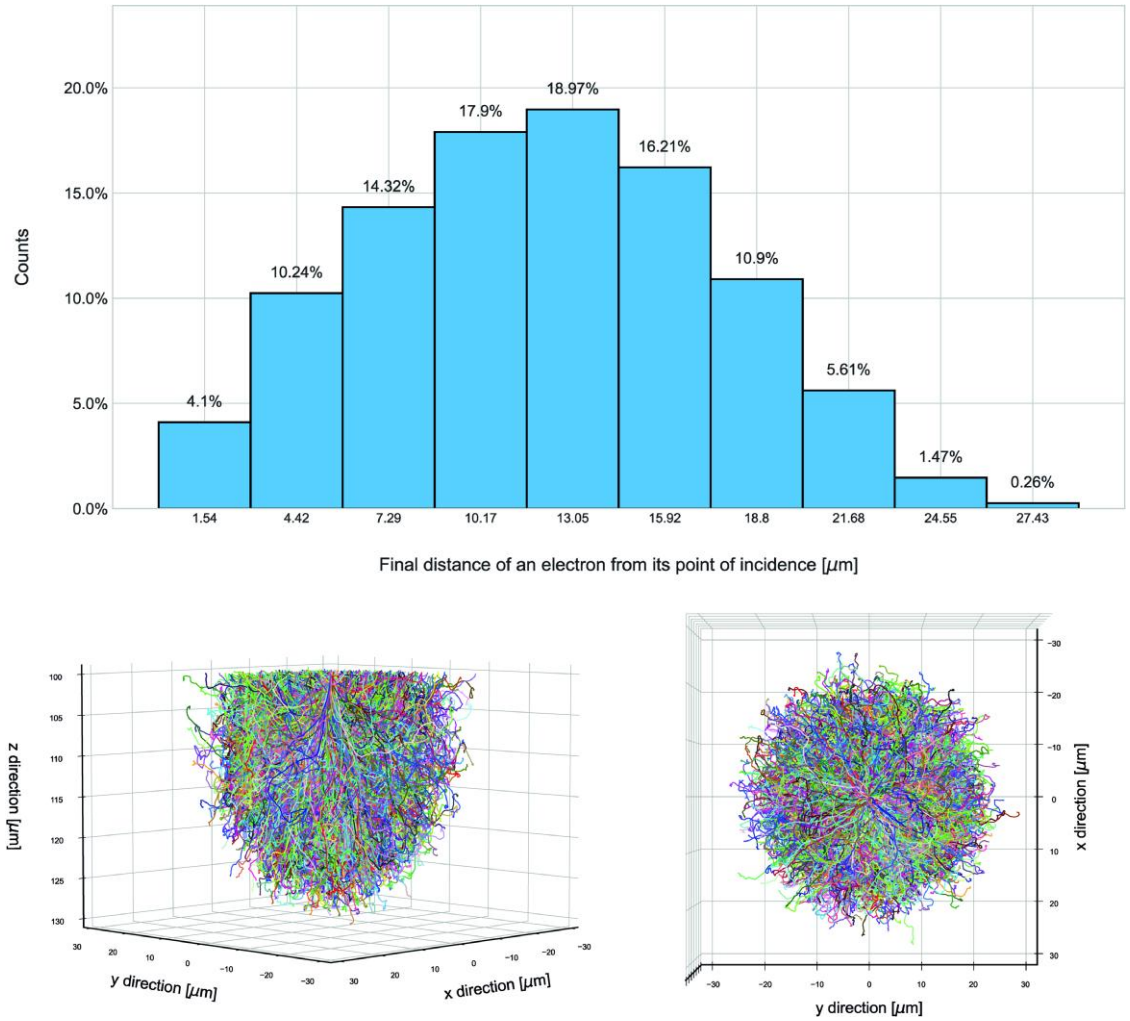

Fig. 6. Histogram of the final distance of an electron from the center of a pixel to show the lateral spread of the 60-keV electrons in silicon; two viewpoints of the trajectories of the 60-keV electrons are shown below the histogram. There are 5,000 trajectories in this simulation; color is randomly assigned to help distinguish between trajectories.

workstation used. InFluence calculations are currently only handled by the CPU.

Results

Application of InFluence on a Simulated Image of an MoS_2 Lattice

We use the Python package abTEM to simulate normalized TEM images of a molybdenum disulphide (MoS_2) lattice. Figure 3 presents simulated 80- and 200-keV normalized TEM images of an MoS_2 lattice surrounded by vacuum. The simulated electron beams are partially spatially and temporally coherent, and the microscope exhibits third order spherical aberrations, C_s. Deflections of the image relative to the detector can occur because of vibrations, stage drift, and thermal magnetic field noise. In abTEM, the contribution of these noise sources is adjusted by the Gaussian spread, G. In abTEM, temporal and spatial coherence are controlled by adjusting the unitless focal spread, δ, and unitless angular spread, β, parameters, respectively. The lattices are imaged at Scherzer defocus, D. For the 80-kV electron simulation, these parameters are as follows: $\delta = 40$, $\beta = 0.5$, $C_s = -7\ \mu$m, $D \approx -66.22$ Å, and $G = 2$ Å. For the 200-kV electron simulation, $\delta = 40$, $\beta = 0.5$, $C_s = -7\ \mu$m, $D \approx -51.32$ Å, and $G = 2$ Å.

Figures 4 and 5 show a set of unmodulated finite fluence MoS_2 lattice images simulated with an 80- and 200-keV electron beam, respectively. The corresponding modulated images and difference images are also shown. The difference images are calculated by subtracting the modulated image from the unmodulated image. The difference images highlight how the intensities change after modulation. In other words, they show the difference between the image plane and detector plane. Figure 4i shows that the intensity differences between the unmodulated and modulated images are negative for 80-keV electrons thresholded at 32 keV. The intensities of the modulated image are higher than those of the unmodulated image because the 80-keV electrons are counted multiple times in the same pixel as a result of the counting threshold used here and since 80-keV electrons tend to not scatter into neighboring pixels. Conversely, 200-keV electrons tend to disperse into neighboring pixels; in fact, 200-keV electrons can scatter to ~4.8 Medipix3 pixels from their point of incidence (see the Evaluating the Implementation of the Single Scattering Model section for more details). Figure 5i shows that counting 200-keV

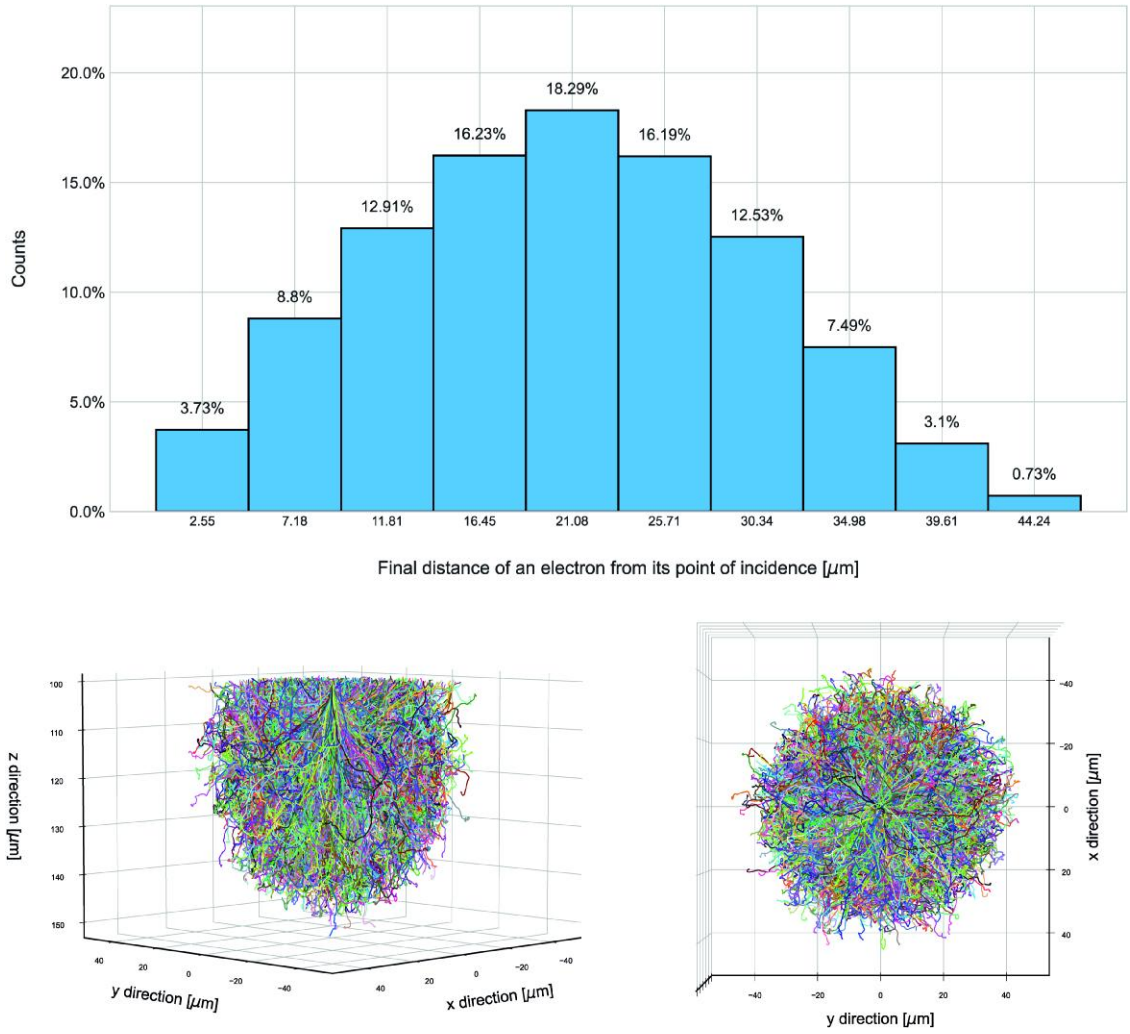

Fig. 7. Histogram of the final distance of an electron from the center of a pixel to show the lateral spread of the 80-keV electrons in silicon; two viewpoints of the trajectories of the 80-keV electrons are shown below the histogram. There are 5,000 trajectories in this simulation; color is randomly assigned to help distinguish between trajectories.

electrons with a 40% threshold results in an underestimation of electron counts and significantly more blurring. Effectively, the impact of modulation on measurements is a reduction in high spatial frequency information, and the magnitude of this reduction becomes more severe as the incident energy increases.

Evaluating the Implementation of the Single Scattering Model

All calculations were performed with standard InFluence, referred to as just InFluence from here onward.

The trajectories of the electrons simulated with our implementation of the single scattering model compared well to those in other literature: the authors of (Mir et al., 2017) used the CASINO software package (Drouin et al., 2007) to calculate the lateral spread of 60- and 80-keV electrons in a silicon pixel, showing that 95% of the electrons travel out to ~25 and 42 μm for 60- and 80-keV electrons, respectively. The histograms in Figures 6 and 7 show that the 5,000 60- and 80-keV electrons simulated using InFluence exhibit a similar lateral spread. Recall from the Medipix3 Specifications section, the Medipix3 sensor layer is 300 μm deep, and the pixels are square with a 55-μm side. Therefore, an electron incident on *the center* of the pixel is unlikely to scatter into a neighboring pixel; note, though, 60- and 80-keV electrons are still likely to scatter into neighboring pixels because electrons can be incident on any part of the pixel. The histogram in Figure 8 shows that a 200-keV electron can travel out to ~265 μm, which is >4.8 Medipix3 pixels from its point of origin. Depending on the value set for T_{counting}, an electron can be counted multiple times across several pixels. To summarize, with high T_{counting}, the modulation of the image is not very significant or apparent because low-energy electrons tend to not scatter into neighboring pixels if they are incident near the center of the pixel. High-energy electrons can travel through several pixels and can be measured many times or not at all depending on the energy transferred in each pixel and the selected T_{counting}, which, as will be shown in the subsequent section, leads to significant contrast modulation of the input image.

Characterization of the Simulated Medipix3

The MTF, NPS and DQE were evaluated in the spatial frequency range from 0 to 0.5, where 0.5 represents the Nyquist frequency. The unmodulated and modulated slanted edge and white noise images are shown in Figures 9 and 10,

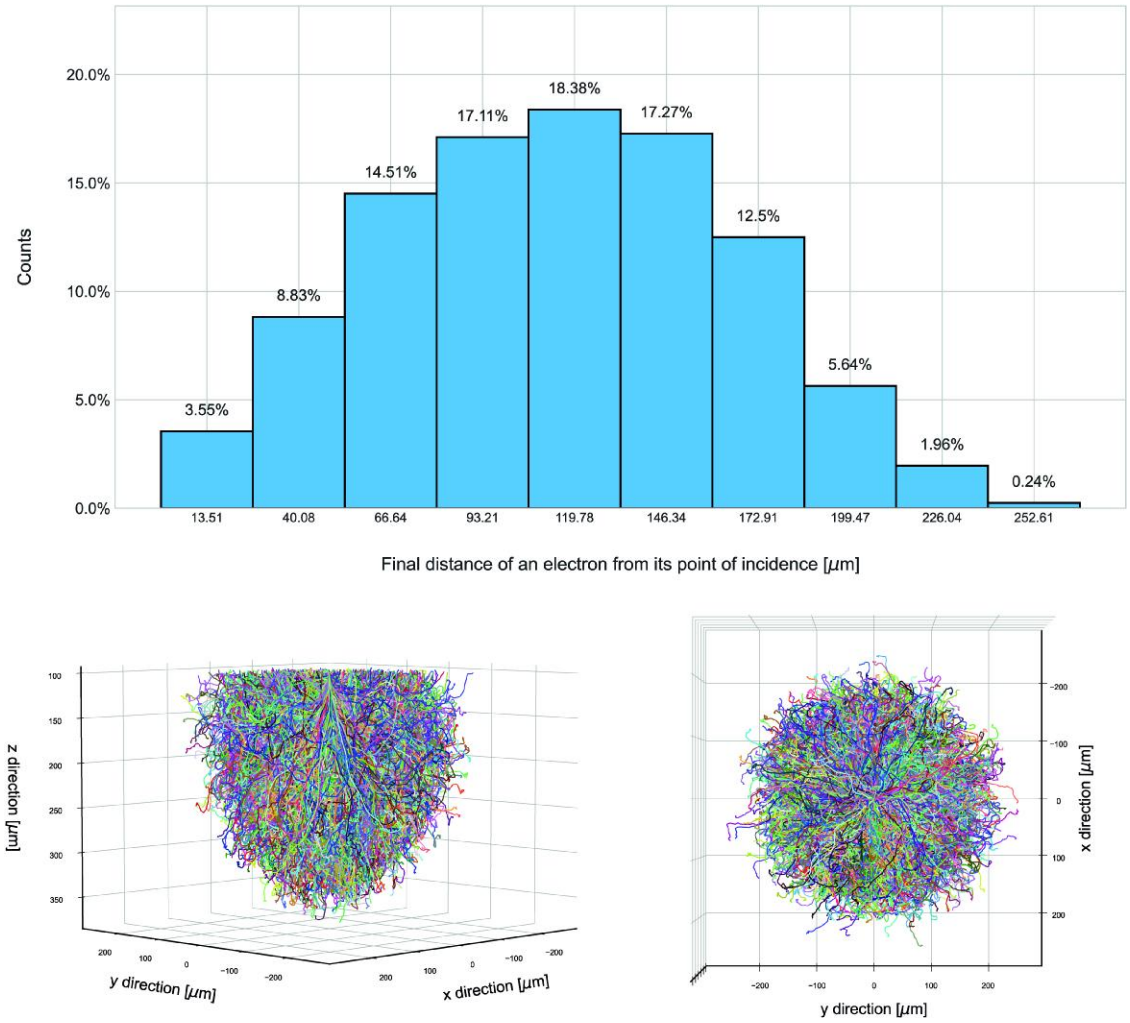

Fig. 8. Histogram of the final distance of an electron from the center of a pixel to show the lateral spread of the 200-keV electrons in silicon; two viewpoints of the trajectories of the 200-keV electrons are shown below the histogram. There are 5,000 trajectories in this simulation; color is randomly assigned to help distinguish between trajectories.

respectively; the images are simulated with different electron fluences: 10 e/pixel and 100 e/pixel. Each edge is oriented at an angle of 0.1 rad to the x-axis, giving an oversampling factor of ~10 times the pixel pitch to ensure that the specified eight sampling bins are nonempty. The edges are imaged with 80 keV and with 200-keV electrons that InFluence thresholds at 32 and 80 keV, respectively. Note that the darkening of the edges of the images arises from the scattering of the electrons outside the finite boundary of the detector. These electrons do not contribute to the image and InFluence does not simulate software postprocessing of the image or detector dead area that might remove or account for these artifacts. Note the distribution of intensities from the white noise images before and after modulation shown in Figure 11; the count change after modulation is +40% for the 80-keV electrons and −50% for 200-keV electrons, despite the energy of the electron–hole pairs generated by both electron beams being thresholded at 40% of the incident beam energy. The narrowing of the 200-keV distribution and the reduction in counts after modulation is indicative that a lower threshold is required to improve DQE, to ensure that electrons that spread their energy to too many neighboring pixels are counted.

These slanted edges and white noise images were used to obtain the MTFs, NPSs, and DQEs shown in Figures 12–15. The MTF degrades with increasing electron energy, which we attribute to the stochastic lateral spread of the electrons in the silicon sensor layer. This lateral spread is the reason the edge becomes blurrier with increasing electron energy, as demonstrated in Figures 9c and 9f.

Figure 12 shows that higher electron fluences result in a smoother MTF, since the fluctuations in the intensity profile across the edge are less significant compared to the average electron fluence. This result is unsurprising because the MTF metric is a statistical quantity, thus requiring an adequately large number of electron counts over a suitable exposure time. The stochastic nature of the electron scattering in the sensor layer means that each electron transfers spatial frequency information differently. MTFs generated from an edge imaged under high electron fluence conditions cannot be used to simulate low electron fluence experiments reliably.

Figures 13 and 14 present the NPS corresponding to the MTFs in Figure 12. A perfectly flat power spectrum normalized to 1 is only expected for an ideal white noise process and unlikely to ever be observed in practice. In general, the degree to which the

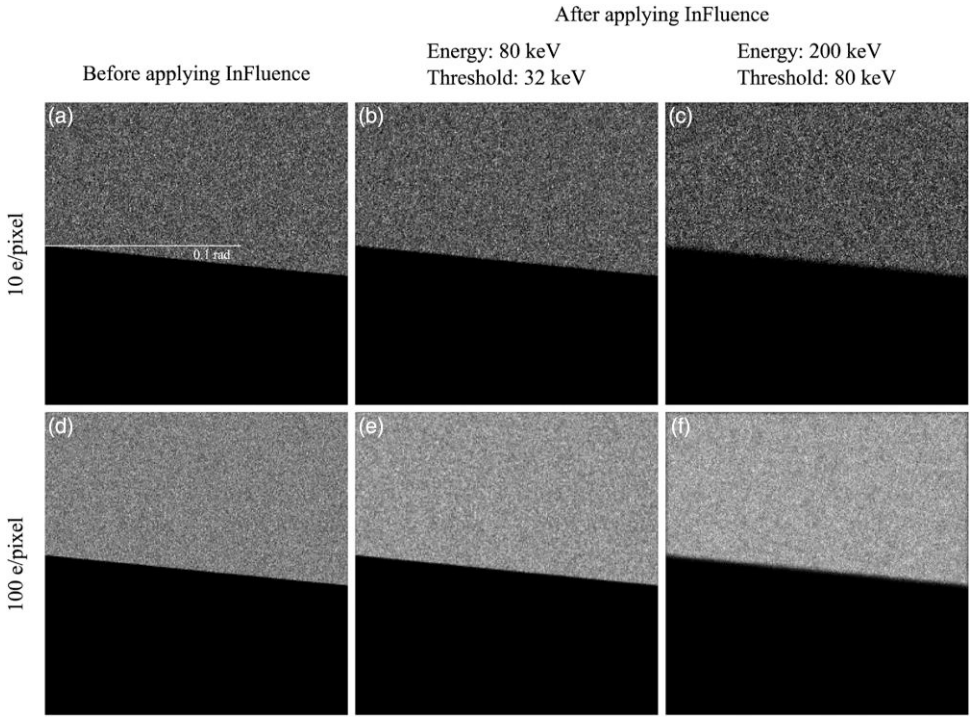

Fig. 9. Simulated slanted edge images, with a slant of 0.1 rad from the horizontal of the image: (**a, d**) before applying InFluence; (**b, e**) after applying InFluence with 80-keV electrons and a 32-keV threshold; (**c, f**) after applying InFluence with 200-keV electrons and an 80-keV threshold. The average electron fluence is 10 e/pixel for (**a**)–(**c**) and 100 e/pixel for (**d**)–(**f**).

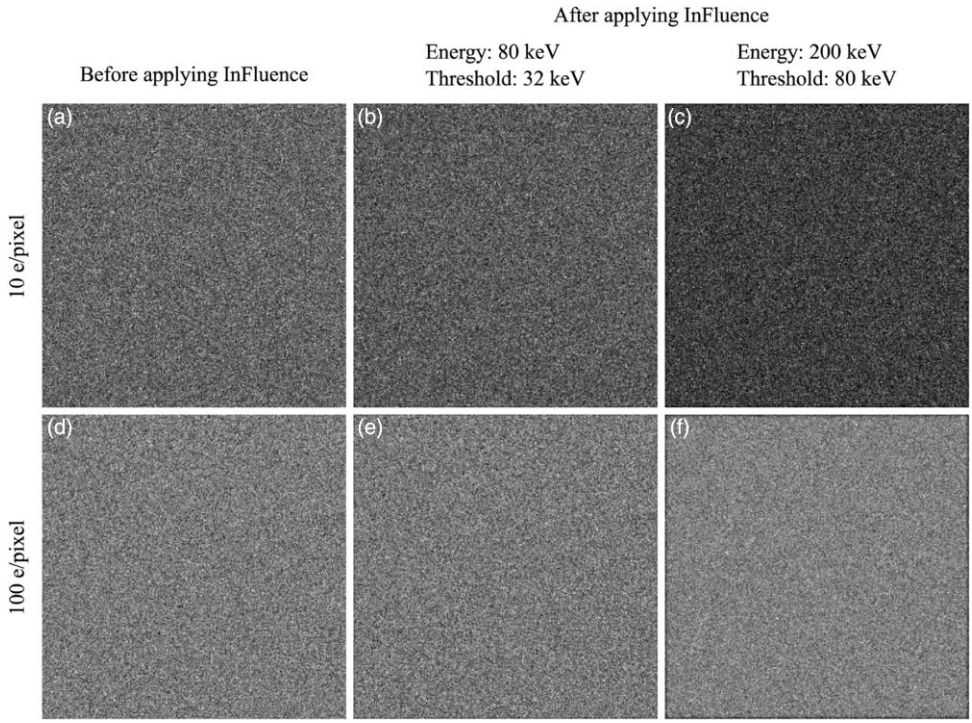

Fig. 10. Simulated white noise images: (**a, d**) before applying InFluence; (**b, e**) after applying InFluence with 80-keV electrons and a 32-keV threshold; (**c, f**) after applying InFluence with 200-keV electrons and an 80-keV threshold. The average electron fluence is 10 e/pixel for (**a**)–(**c**) and 100 e/pixel for (**d**)–(**f**).

power of noise decreases for higher spatial frequencies is more severe for 200-keV electrons than that for the 80-keV electrons. This is further evidence that the lateral spread of the electrons strongly impacts the measured noise.

We present the simulated DQEs under low and high electron fluence conditions and the ideal DQE according to Equation (32). Since the DQE, MTF, and NPS are related through Equation (30), Figure 15 serves to reiterate the points

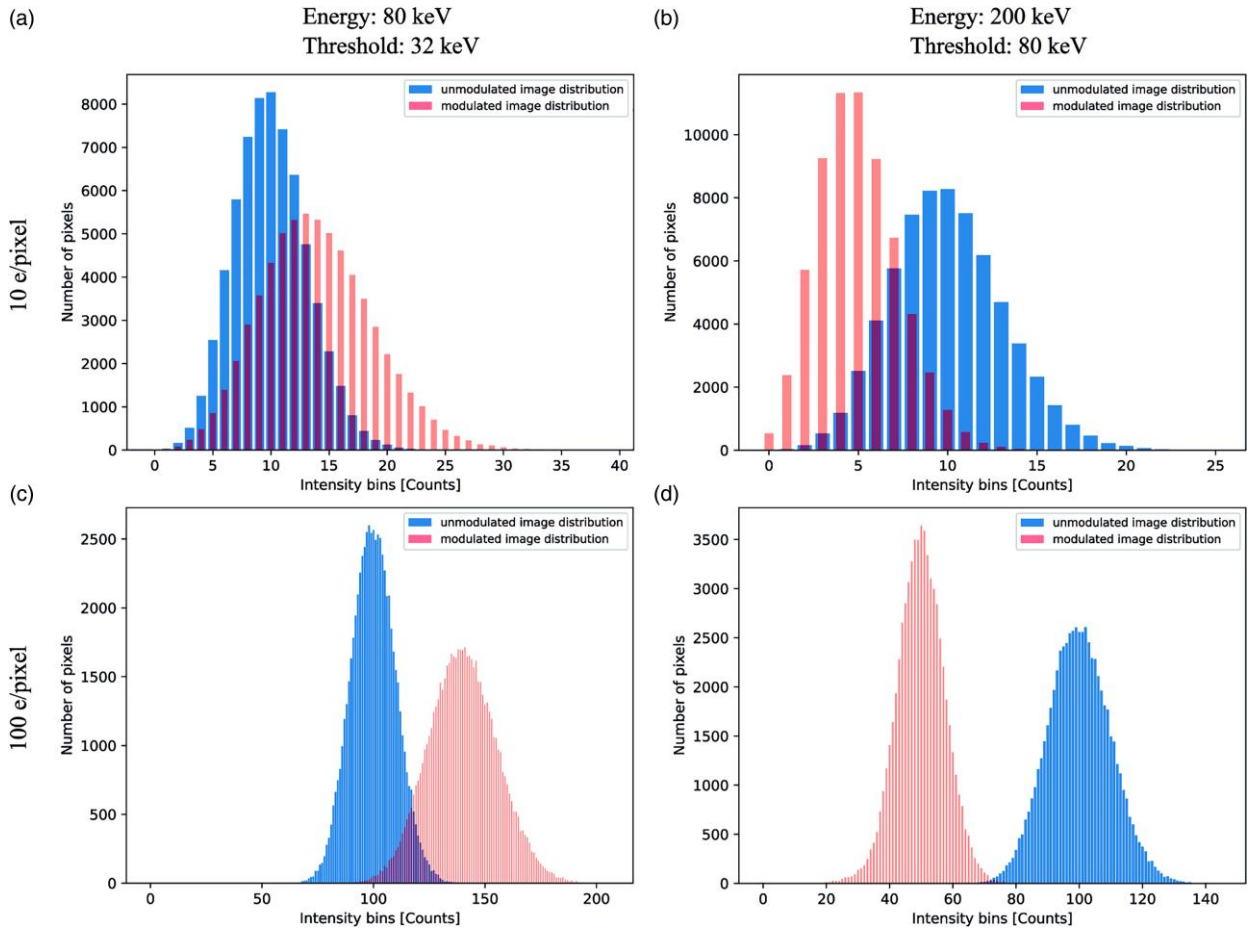

Fig. 11 Modulated and unmodulated image distributions for (**a, c**) 80-keV electrons with a 32-keV threshold, (**b, d**) 200-keV electrons with an 80-keV threshold. The average electron fluence is 10 e/pixel for (**a**) and (**b**) and 100 e/pixel for (**c**) and (**d**).

made above. That is, each electron exhibits a unique DQE; therefore, DQEs generated from high electron fluence data cannot be used to simulate low electron fluence experiments reliably.

Presented so far are the results for electrons thresholded at 40% of their incident energy. Figure 17 shows that a higher threshold decreases the relative maximum magnitude of the DQE because the energy of the electron–hole pairs generated by the propagating electrons is less likely to exceed the threshold. Careful consideration must be made to maximize the DQE while minimizing the blurring associated with the lateral spread of electrons into neighboring pixels; that is, there is a trade-off between maximizing the DQE and MTF. In the case of low fluence cryo-EM experiments, in which the electron fluence is typically on the order of 10 s e/Å^2, a high DQE is prioritized over a better MTF to maximize the measured signal. Note, as shown by considering Figures 16 and 17, an increased threshold improves the MTF but not as dramatically as it reduces the DQE.

Comparison to Physical Experiments

Figure 18 is a plot comparing simulated and experimental MTFs obtained from images recorded with 60-keV electrons thresholded at 5.6, 37.0, and 51.9 keV. We obtained the MTFs from Figure A.3, reproduced from Mir et al. (2017), and multiplied them by sinc(f) for comparison with our 2D MTF trend lines. For all simulations, the average fluence is ~40,000 electrons per pixel, leading to smoother curves typically obtained in experimental MTFs. The simulated ideal detector compares well with the expected ideal frequency response: the sinc^2(f) function. The experimental and simulated MTFs obtained with a 5.6-keV threshold are the only trend lines that compare well. The simulated MTFs for 37.0- and 51.9-keV thresholds fall predict weaker frequency responses for higher spatial frequencies than those observed by Mir et al. There are two likely reasons for this: (i) the calibration of the real Medipix3 detector could mean that the thresholds used in experiment are not completely comparable those used in simulation. (ii) The uniform distribution of electrons on *every* pixel surface is erroneous. The pixels near the edge object are only partially exposed to the electron beam, implying that a more sophisticated distribution method is necessary to improve the model of the detector. The most obvious way to solve this problem is to oversample the detector pixels and then bin the output image to the desired detector size. Regardless, the improper use of a uniform distribution at the edge explains why the simulated MTF exhibits more severe degradation at higher spatial frequencies. Reiterating, the MTF characterizes the spread of electrons from the pixel on which they impinge. The improper use of a uniform distribution of electron on pixels along the edge allows some of the electrons to impinge too close to the region blocked by the edge object. This increases the blurring effect arising from lateral scattering.

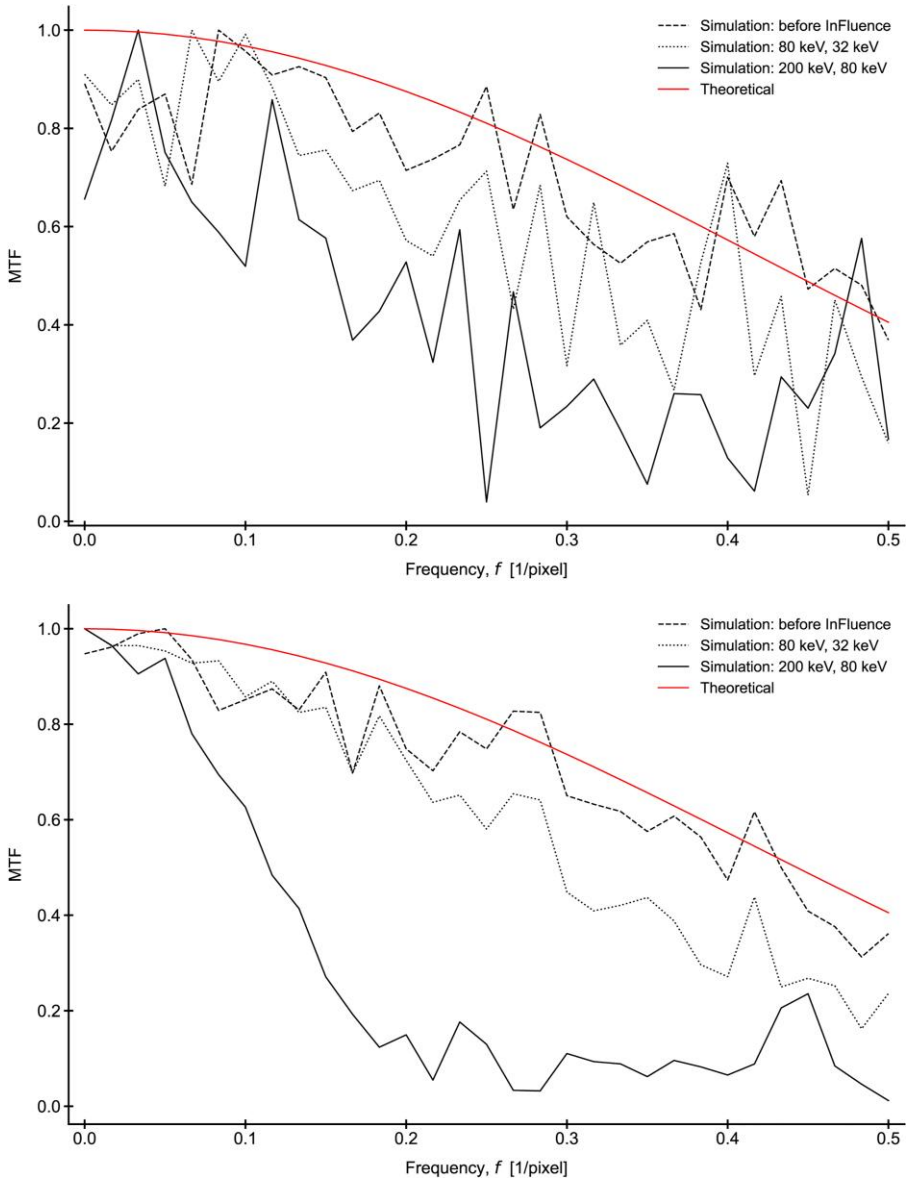

Fig. 12 MTF as a function of spatial frequency for a simulated slanted edge simulated without applying InFluence, with an 80-keV electron energy and 32-keV threshold and with a 200-keV electron energy and 80-keV threshold. The theoretical curve is modeled using Equation (A.7). The top and bottom plot are generated from slanted edge images with an average electron fluence of 10 and 100 e/pixel, respectively.

Conclusions

The motivation for making InFluence was to provide an open and user-friendly software to simulate image modulation due to detector–electron interactions. InFluence is flexible enough to allow the user to adjust the simulated sensor layer and beam properties. InFluence is reasonably fast on a single CPU core but activating parallel mode or refactoring the code to run on a GPU would further reduce the calculation time. Reductions to the calculation time at the cost of increased uncertainty can also be realized by loading a sample distribution of possible electron trajectories instead of calculating the full paths of every electron in real time.

Comprehensive analysis of a simulated Medipix3 detector produced results that compared well to expectations and to those presented in literature. That is, the choice of accelerating voltage and energy threshold plays an important role on the MTF and DQE. Generally, high-energy electrons will disperse to neighboring pixels, reducing the MTF at high spatial frequencies; a high threshold will improve the MTF, but to the detriment of the DQE. Results showed that the characterization methods used are appropriate for high fluence experiments, where the SNR is sufficiently large. Low fluence MTFs and DQEs were noisy across all spatial frequencies, with an increase in fluence resulting in smoother curves.

Current understanding of the Stobbs factor indicates that its origin is instrument relate (Juri Barthel et al., 2017). Accounting for the effect of the detector on the observed image intensities in simulation by application of an empirical MTF rectifies the discrepancy between experiment and simulation (Thust, 2009). Beyond the scope of this paper, further investigation is required to substantiate InFluence as a sufficiently accurate alternative to using empirical MTF files. Such an investigation would include a systematic comparison of experimental images to images simulated with InFluence with the scope of helping to reduce the Stobb's factor and generally

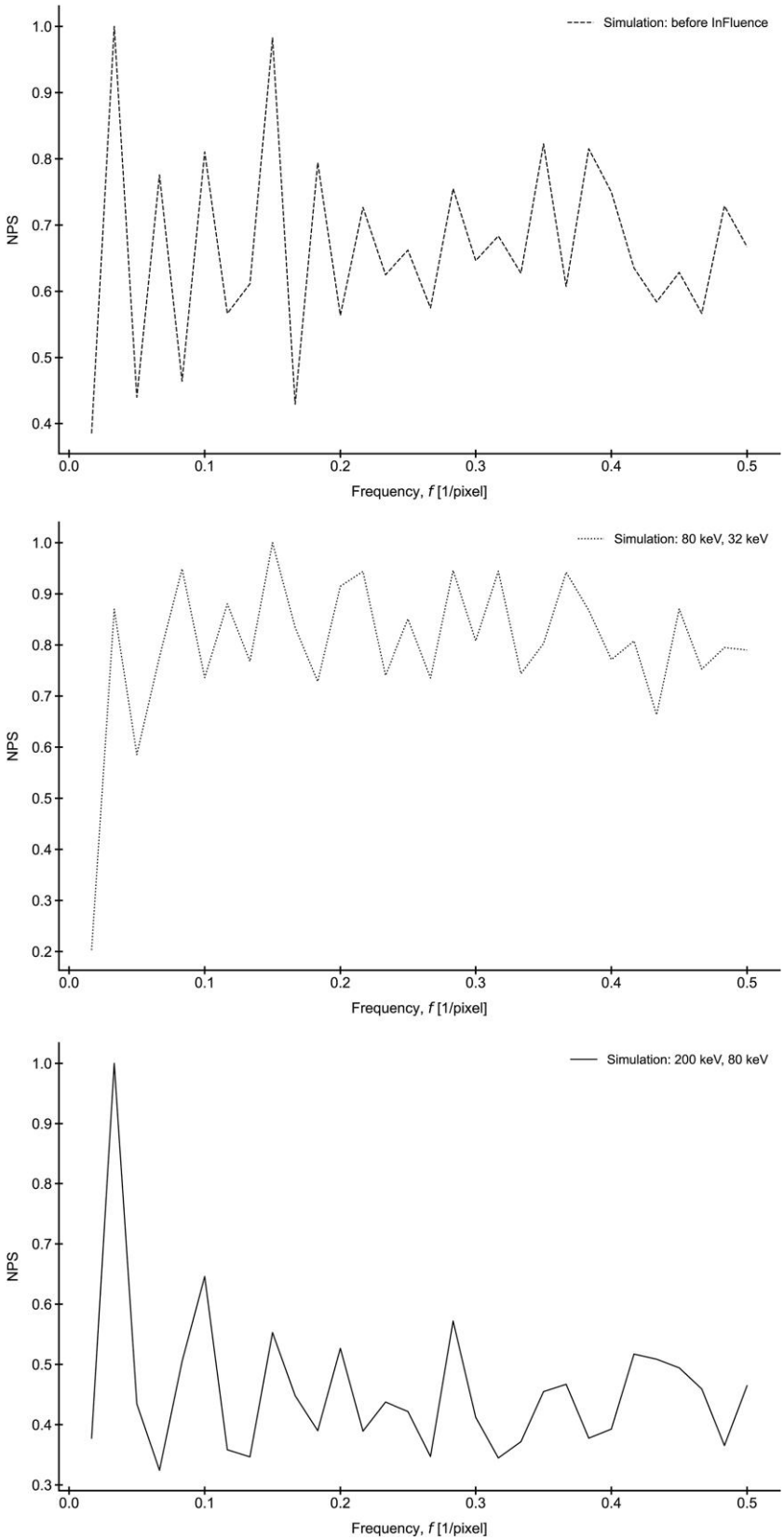

Fig. 13. NPS as a function of spatial frequency for a flat-field field image simulated (top) without applying InFluence, (middle) with an 80-keV electron energy and 32-keV threshold and (bottom) with a 200-keV electron energy and 80-keV threshold. Each plot is generated from white noise images with an average electron fluence of 10 e/pixel. The expected power at each frequency is 1.

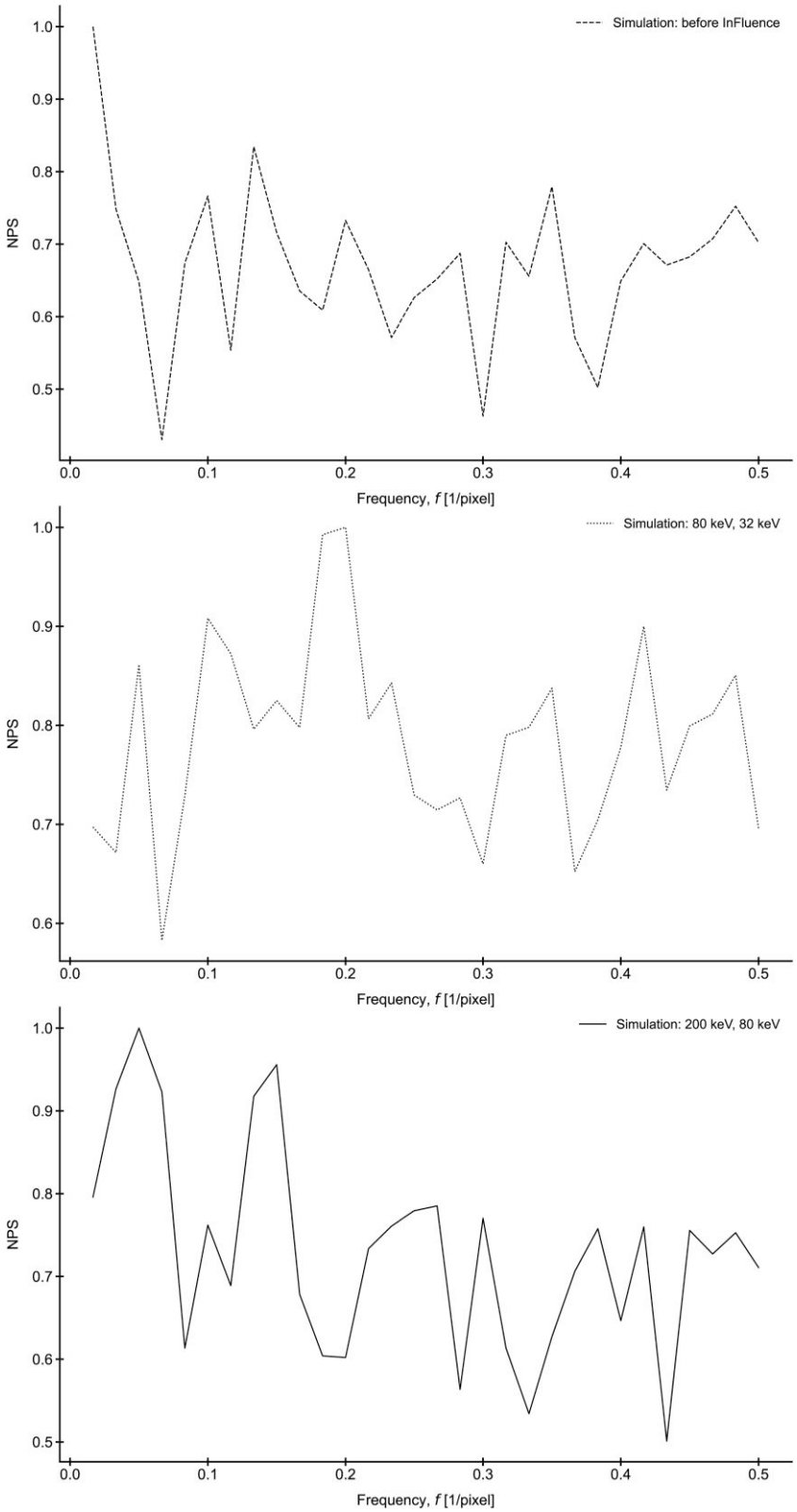

Fig. 14. NPS as a function of spatial frequency for a flat-field field image simulated (top) without applying InFluence, (middle) with an 80-keV electron energy and 32-keV threshold and (bottom) with a 200-keV electron energy and 80-keV threshold. Each plot is generated from a white noise image with an average electron fluence of 100 e/pixel. The expected power at each frequency is 1.

improve the quality of TEM image and diffraction simulation, which would reduce the error between simulation and experimental data. InFluence is freely available to be used in conjunction with any existing multislice simulation software, with the aim of aiding researchers in applying TEM simulations to a wider array of experimental conditions where the beam fluence can be used as an experimental parameter within the simulations to determine appropriate beam and fluence conditions for use in

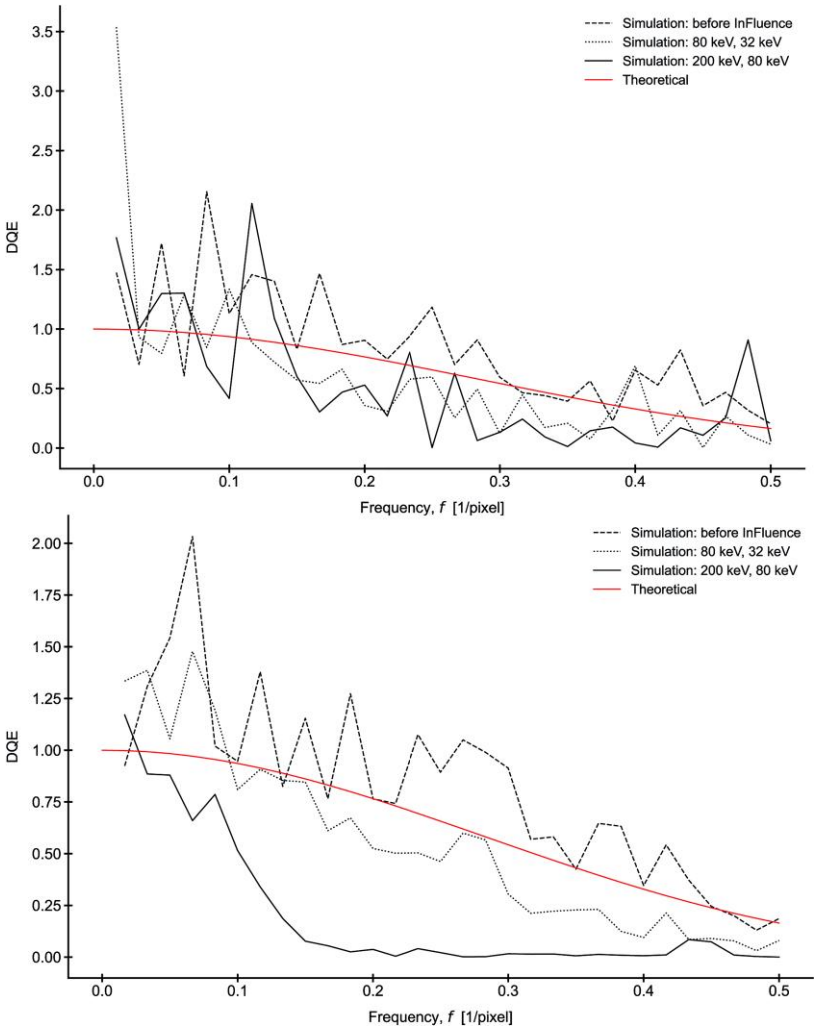

Fig. 15. DQE as a function of spatial frequency simulated without applying InFluence, with a 80-keV electron energy and 32-keV threshold and with a 200-keV electron energy and 80-keV threshold. The theoretical curve is modeled using Equation (A.10). The top and bottom DQEs are calculated from MTFs and NPSs generated from images that were both simulated with an average electron fluence of 10 and 100 e/pixel, respectively.

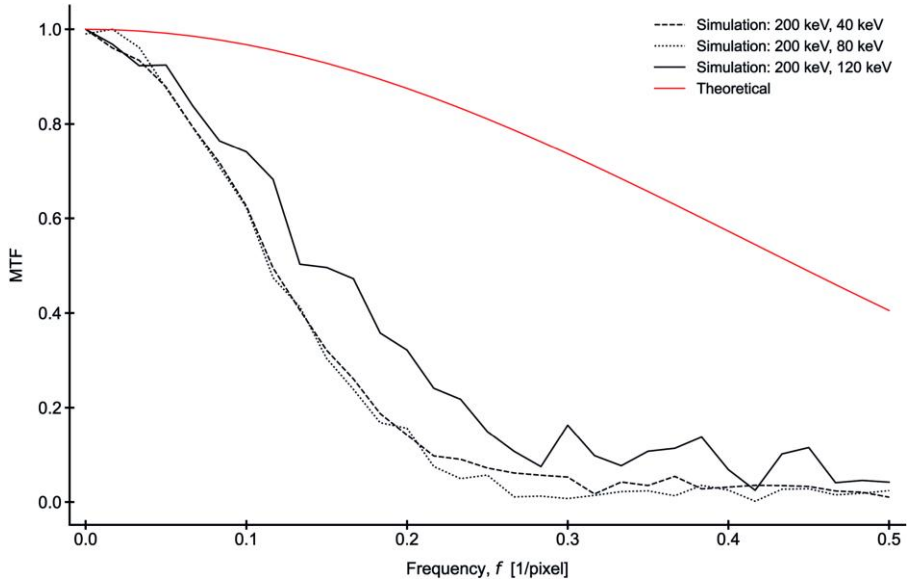

Fig. 16. MTF as a function of spatial frequency simulated for 200-keV electrons with 40-, 80-, and 120-keV thresholds. The theoretical curve is modeled using Equation (A.7). The plot is generated from a slanted edge image with an average electron fluence of 1,000 e/pixel.

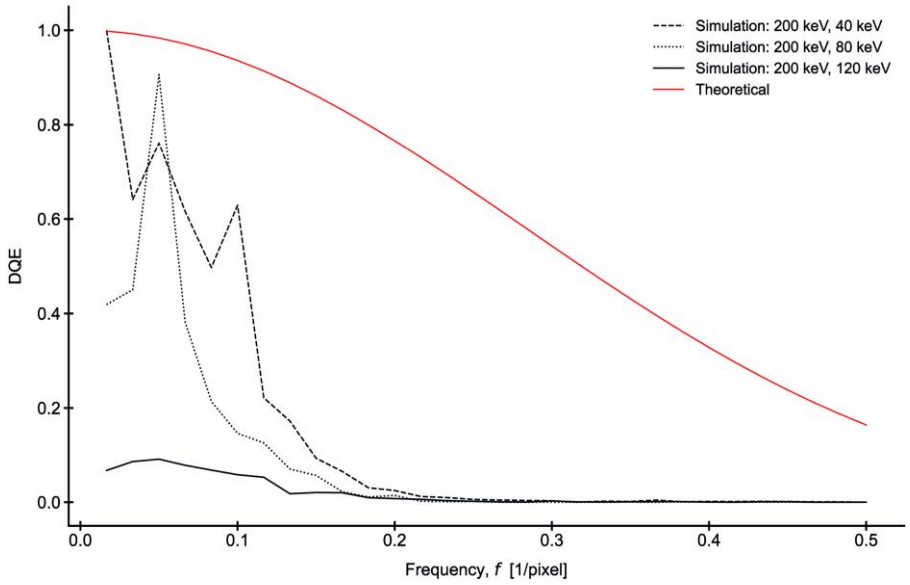

Fig. 17. DQE as a function of spatial frequency simulated for 200-keV electrons with 40-, 80-, and 120-keV thresholds. The theoretical curve is modeled using Equation (A.10). The plot is calculated from an MTF and NPS generated from images that were both simulated with an average electron fluence of 1,000 e/pixel.

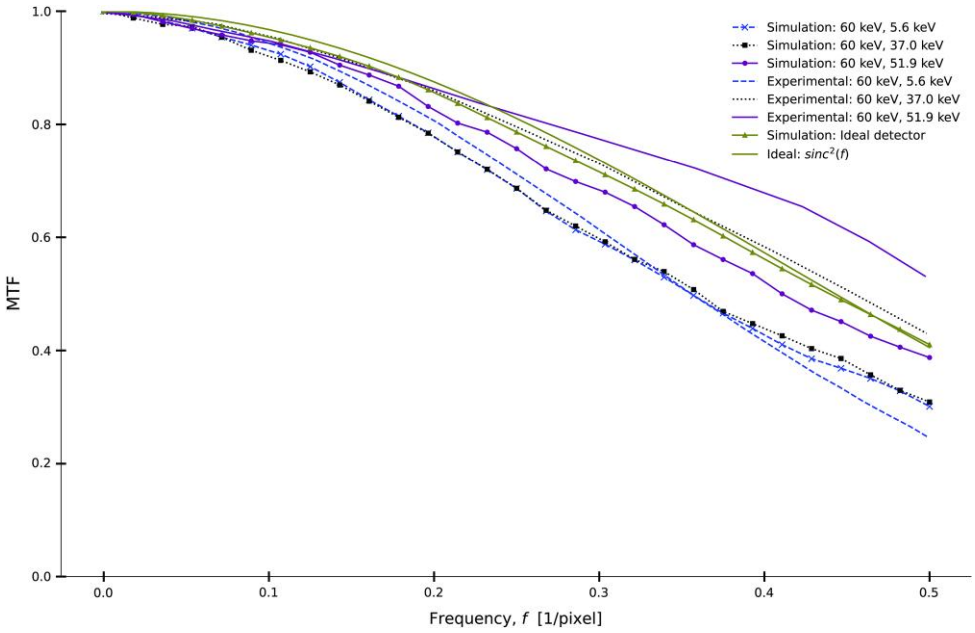

Fig. 18. Experimental and simulated MTF for the Medipix3 operating in SPM, obtained for 60 and 80 electrons with various values of $T_{counting}$. The data from Figure A.3 has been multiplied by the sinc(f) function for a better comparison to our 2D (for square pixels) MTF trend lines.

experiments and to optimize signal-to-noise for beam sensitive materials in (S)TEM experiments, as well as enabling more traditional image simulation applications of qualitative image matching for low electron beam fluence experiments.

Availability of Data and Materials

The standard and alternative versions of InFluence are available in this GitHub repository under two separate branches: https://github.com/AMCLab/InFluence. Additionally, we provide a normalized image of a monolayer MoS_2 lattice and a slanted edge object for testing.

Acknowledgments

The authors are grateful to Dr. Ian Clancy for fruitful discussions on the single scattering model and to Dr. Gary Patterson for his insights on the Medipix3 detector. The authors also acknowledge Eoin Walsh and David Landers for providing support and coding advice.

Financial Support

This work was supported by the Physics Department and the Bernal Institute at the University of Limerick, Limerick, Ireland.

Conflict of Interest

The authors declare no competing interests.

References

Ahmed SN (2015). *7—Position-Sensitive Detection and Imaging*, S. N. B. T.-P. and E. of R. D. Second E. Ahmed (Eds.), pp. 435–475. Amsterdam, Netherlands: Elsevier. https://doi.org/10.1016/B978-0-12-801363-2.00007-3

Ballabriga R, Campbell M, Heijne E, Llopart X, Tlustos L & Wong W (2011). Medipix3: A 64k pixel detector readout chip working in single photon counting mode with improved spectrometric performance. *Nucl Instrum Methods Phys Res Sec A* **633**, S15–S18. https://doi.org/10.1016/j.nima.2010.06.108

Ballabriga R, Campbell M & Llopart X (2018). Asic developments for radiation imaging applications: The medipix and timepix family. *Nucl Instrum Methods Phys Res Sec A* **878**, 10–23. https://doi.org/10.1016/j.nima.2017.07.029

Barthel J (2018). Dr. Probe: A software for high-resolution STEM image simulation. *Ultramicroscopy* **193**, 1–11. https://doi.org/10.1016/j.ultramic.2018.06.003

Barthel J, Lentzen M & Thust A (2017). On the influence of the electron dose rate on the HRTEM image contrast. *Ultramicroscopy* **176**, 37–45. http://dx.doi.org/10.1016/j.ultramic.2016.11.016

Berger MJ, Inokuti M, Anderson HH, Bichsel H, Dennis JA, Powers D, Seltzer SM & Turner JE (1984). Report 37. *J Int Commission Radiat Units Meas* **os19**(2), NP–NP. https://doi.org/10.1093/jicru/os19.2.Report37

Booth C (2012). K2: A super-resolution electron counting direct detection camera for cryo-EM. *Microsc Microanal* **18**(S2), 78–79. https://doi.org/10.1017/S1431927612002243

Browning R (1991). Universal elastic scattering cross sections for electrons in the range 1–100 keV. *Appl Phys Lett* **58**(24), 2845–2847. https://doi.org/10.1063/1.104754

Carlson DB & Evans JE (2012). Low-Dose imaging techniques for transmission electron microscopy. In *The Transmission Electron Microscope*, Maaz K (Ed.), pp. 85–98. London, England: IntechOpen.

Cautaerts N, Crout P, Ånes HW, Prestat E, Jeong J, Dehm G & Liebscher CH (2022). Free, flexible and fast: Orientation mapping using the multi-core and GPU-accelerated template matching capabilities in the python-based open source 4D-STEM analysis toolbox pyxem. *Ultramicroscopy* **237**(113517). https://doi.org/10.1016/j.ultramic.2022.113517

Chen Q, Dwyer C, Sheng G, Zhu C, Li X, Zheng C & Zhu Y (2020). Imaging beam-sensitive materials by electron microscopy. *Adv Mater* **32**(16), 1907619. https://doi.org/10.1002/adma.201907619

Clabbers MTB, van Genderen E, Wan W, Wiegers EL, Gruene T & Abrahams JP (2017). Protein structure determination by electron diffraction using a single three-dimensional nanocrystal. *Acta Crystallogr Sec D Struct Biol* **73**(Pt 9), 738–748. https://doi.org/10.1107/S2059798317010348

Clausen A, Weber D, Ruzaeva K, Migunov V, Baburajan A, Bahuleyan A, Bryan M, Caron J, Chandra R, Dey S, Halder S, Katz DS, Levin BDA, Nord M, Ophus C, Peter S, Puskas L, Schyndel van J, Shin J, Sunku S, Müller-Caspary K & Dunin-Borkowski RE (2021). *LiberTEM/LiberTEM: 0.8.0*. Zenodo. https://doi.org/10.5281/zenodo.5547992.

Czyżewski Z, MacCallum DO, Romig A & Joy DC (1990). Calculations of mott scattering cross section. *J Appl Phys* **68**(7), 3066–3072. https://doi.org/10.1063/1.346400

de la Pena F, Prestat E, Fauske VT, Burdet P, Lahnemann J, Furnival T, Jokubauskas P, Nord M, Ostasevicius T, MacArthur KE, Johnstone DN, Sarahan M, Aarholt T, Taillon J, pquinn-dls , Migunov V, Eljarrat A, Caron J, Poon T, Mazzucco S, Francis C, Martineau B, Somnath S, Slater T, Tappy N, Walls M, Cautaerts N, Winkler F & DENSmerijn (2021). *hyperspy/hyperspy: Release v1.6.5*. Zenodo. https://doi.org/10.5281/zenodo.5608741

Drouin D, Couture AR, Joly D, Tastet X, Aimez V & Gauvin R (2007). CASINO V2.42—A fast and easy-to-use modeling tool for scanning electron microscopy and microanalysis users. *Scanning* **29**(3), 92–101. https://doi.org/10.1002/sca.20000

Egerton RF (2019). Radiation damage to organic and inorganic specimens in the TEM. *Micron* **119**, 72–87. https://doi.org/10.1016/j.micron.2019.01.005

Fan X, Wang J, Zhang X, Yang Z, Zhang J-C, Zhao L, Peng H-L, Lei J & Wang H-W (2019). Single particle cryo-EM reconstruction of 52 kDa streptavidin at 3.2 Angstrom resolution. *Nat Commun* **10**(1), 2386. https://doi.org/10.1038/s41467-019-10368-w

Feathers JR, Spoth KA & Fromme JC (2021). Experimental evaluation of super-resolution imaging and magnification choice in single-particle cryo-EM. *J Struct Biol X* **5**, 100047. https://doi.org/10.1016/j.yjsbx.2021.100047

Fernandez-Perez S, Boccone V, Broennimann C, Disch C, Piazza L, Radicci V, Rissi M, Schulze-Briese C, Trueb P & Zambon P (2021). Characterization of a hybrid pixel counting detector using a silicon sensor and the {IBEX} readout {ASIC} for electron detection. *J Instrum* **16**(10), P10034. https://doi.org/10.1088/1748-0221/16/10/p10034

Fröjdh E, Bisello F, Campbell M, Damet J, Hamann E, Koenig T, Wong WS & Zuber M (2015). Spectral response of the energy-binning Dosepix ASIC coupled to a 300μm silicon sensor under high fluxes of synchrotron radiation. *Nucl Instrum Methods Phys Res Sec A* **804**, 43–49. https://doi.org/10.1016/j.nima.2015.09.018

Fujiyoshi Y (2013). Low dose techniques and cryo-electron microscopy. *Methods Mol Biol (Clifton, N.J.)* **955**, 103–118. https://doi.org/10.1007/978-1-62703-176-9_6

Gemmi M, Mugnaioli E, Gorelik TE, Kolb U, Palatinus L, Boullay P, Hovmöller S & Abrahams JP (2019). 3D Electron diffraction: The nanocrystallography revolution. *ACS Cent Sci* **5**(8), 1315–1329. https://doi.org/10.1021/acscentsci.9b00394

Gruene T & Mugnaioli E (2021). 3D Electron diffraction for chemical analysis: Instrumentation developments and innovative applications. *Chem Rev* **121**(19), 11823–11834. https://doi.org/10.1021/acs.chemrev.1c00207

Guo H, Franken E, Deng Y, Benlekbir S, Singla Lezcano G, Janssen B, Yu L, Ripstein ZA, Tan YZ & Rubinstein JL (2020). Electron-event representation data enable efficient cryoEM file storage with full preservation of spatial and temporal resolution. *IUCrJ* **7**(5), 860–869. https://doi.org/10.1107/S205225252000929X

Howie A (2004). Hunting the Stobbs factor. *Ultramicroscopy* **98**(2–4), 73–79. http://dx.doi.org/10.1016/j.ultramic.2003.08.002

Hunter JD (2007). Matplotlib: A 2D graphics environment. *Comput Sci Eng* **9**(3), 90–95. https://doi.org/10.1109/MCSE.2007.55

Jia C-L, Barthel J, Gunkel F, Dittmann R, Hoffmann-Eifert S, Houben L, Lentzen M & Thust A (2013a). Atomic-Scale measurement of structure and chemistry of a single-unit-cell layer of LaAlO3 embedded in SrTiO3. *Microsc Microanal* **19**(2), 310–318. https://doi.org/10.1017/S1431927612014407

Jia CL, Mi SB, Barthel J, Wang DW, Dunin-Borkowski RE, Urban KW & Thust A (2014b). Determination of the 3D shape of a nanoscale crystal with atomic resolution from a single image. *Nat Mater* **13**-(11), 1044–1049. https://doi.org/10.1038/nmat4087

Joy DC (1995). *Monte Carlo Modelling for Electron Microscopy and Microanalysis*, 1st ed. pp. 3–55. Oxford, England: Oxford University Press.

Jyoti Bora D (2021). Chapter 9—Contrast improvement of medical images using advanced fuzzy logic-based technique. In *Hybrid Computational Intelligence for Pattern Analysis and Understanding*, Gandhi T, Bhattacharyya S, De S, Konar D (Eds.), S. B. T.-A. M. V. P. for M. I. A. Dey (Eds.), pp. 229–257. Cambridge, MA: Academic Press. https://doi.org/10.1016/B978-0-12-819295-5.00009-3

Kirkland EJ (2020). *Theory of Calculation of Images of Thick Specimens BT—Advanced Computing in Electron Microscopy*. Kirkland EJ (Ed.), pp. 143–195. Cham, Switzerland: Springer

International Publishing. https://doi.org/10.1007/978-3-030-33260-0_6
Kohm K (2004). Modulation transfer function measurement method and results for the orbview-3 high resolution imaging satellite. *Proc. Geo-Imagery Bridging Continents XXth ISPRS Congr.* **35**, 7–12.
Lam SK, Pitrou A & Seibert S (2015). Numba: A LLVM-based python JIT compiler. *Proceedings of the Second Workshop on the LLVM Compiler Infrastructure in HPC—LLVM '15* 1–6. https://doi.org/10.1145/2833157.2833162
Li X, Mooney P, Zheng S, Booth CR, Braunfeld MB, Gubbens S, Agard DA & Cheng Y (2013). Electron counting and beam-induced motion correction enable near-atomic-resolution single-particle cryo-EM. *Nat Methods* **10**(6), 584–590. https://doi.org/10.1038/nmeth.2472
Li H, Yan C & Shao J (2016). Measurement of the modulation transfer function of infrared imaging system by modified slant edge method. *J Opt Soc Korea* **20**(3), 381–388. https://doi.org/1
Lobato I & Van Dyck D (2015). MULTEM: A new multislice program to perform accurate and fast electron diffraction and imaging simulations using graphics processing units with CUDA. *Ultramicroscopy* **156**, 9–17. https://doi.org/10.1016/j.ultramic.2015.04.016
Lowney, J. R., Marx, E., & Under Secretary for Technology National Institute of Standards and Technology (1994). *User's manual for the program MONSEL-1*. https://doi.org/10.6028/NIST.SP.400-95
Madsen J & Susi T (2021). The abTEM code: Transmission electron microscopy from first principles [version 2; peer review: 2 approved]. *Open Res Eur* **1**, 24. https://doi.org/10.12688/openreseurope.13015.2
Masaoka K (2018). Accuracy and precision of edge-based modulation transfer function measurement for sampled imaging systems. *IEEE Access* **6**, 41079–41086. https://doi.org/10.1109/ACCESS.2018.2856742
Masaoka K, Yamashita T, Nishida Y & Sugawara M (2014). Modified slanted-edge method and multidirectional modulation transfer function estimation. *Opt Express* **22**(5), 6040. https://doi.org/10.1364/oe.22.006040
McMullan G, Chen S, Henderson R & Faruqi AR (2009). Detective quantum efficiency of electron area detectors in electron microscopy. *Ultramicroscopy* **109**(9), 1126–1143. https://doi.org/10.1016/j.ultramic.2009.04.002
Mir JA, Clough R, MacInnes R, Gough C, Plackett R, Shipsey I, Sawada H, MacLaren I, Ballabriga R, Maneuski D, O'Shea V, McGrouther D & Kirkland AI (2017). Characterisation of the medipix3 detector for 60 and 80 keV electrons. *Ultramicroscopy* **182**, 44–53. https://doi.org/10.1016/j.ultramic.2017.06.010
Nakane T, Kotecha A, Sente A, McMullan G, Masiulis S, Brown PMGE, Grigoras IT, Malinauskaite L, Malinauskas T, Miehling J, Uchański T, Yu L, Karia D, Pechnikova EV, de Jong E, Keizer J, Bischoff M, McCormack J, Tiemeijer P & Scheres SHW (2020). Single-particle cryo-EM at atomic resolution. *Nature* **587**(7832), 152–156. https://doi.org/10.1038/s41586-020-2829-0
National Research Council (1964). Studies in penetration of charged particles in matter. In *Studies in Penetration of Charged Particles in Matter*. The National Academies Press. https://doi.org/10.17226/20066
Nord M, Vullum PE, MacLaren I, Tybell T & Holmestad R (2017). Atomap: A new software tool for the automated analysis of atomic resolution images using two-dimensional Gaussian fitting. *Adv Struct Chem Imaging* **3**(1), 9. https://doi.org/10.1186/s40679-017-0042-5
O'Connell E, Hennessy M & Moynihan E (2022). PinkShnack/TEMUL. *Zenodo*. Available at https://doi.org/10.5281/zenodo.6338721 (retrieved May 31, 2023).
Oliphant TE (2006). *A Guide to NumPy*, **vol. 1**. USA: Trelgol Publishing.
Ophus C (2017). A fast image simulation algorithm for scanning transmission electron microscopy. *Adv Struct Chem Imaging* **3**(1), 13. https://doi.org/10.1186/s40679-017-0046-1
Ophus C (2019). Four-dimensional scanning transmission electron microscopy (4D-STEM): From scanning nanodiffraction to ptychography and beyond. *Microsc Microanal* **25**(3), 563–582. https://doi.org/10.1017/S1431927619000497
Paterson GW, Lamb RJ, Ballabriga R, Maneuski D, O'Shea V & McGrouther D (2020). Sub-100 nanosecond temporally resolved imaging with the Medipix3 direct electron detector. *Ultramicroscopy* **210**, 112917. https://doi.org/10.1016/j.ultramic.2019.112917
Pryor A, Ophus C & Miao J (2017). A streaming multi-GPU implementation of image simulation algorithms for scanning transmission electron microscopy. *Adv Struct Chem Imaging* **3**(1), 15. https://doi.org/10.1186/s40679-017-0048-z
Rangel DaCosta L, Brown HG, Pelz PM, Rakowski A, Barber N, O'Donovan P, McBean P, Jones L, Ciston J, Scott MC & & Ophus C (2021). Prismatic 2.0—Simulation software for scanning and high resolution transmission electron microscopy (STEM and HRTEM). *Micron* **151**, 103141. https://doi.org/10.1016/j.micron.2021.103141
Rodenburg JM (2008). *Ptychography and Related Diffractive Imaging Methods*, B. T.-A. in I. & E.P. Hawkes (eds.), pp. 87–184, **vol. 150**. Amsterdam, Netherlands: Elsevier. https://doi.org/10.1016/S1076-5670(07)00003-1
S'ari M, Cattle J, Hondow N, Brydson R & Brown A (2019). Low dose scanning transmission electron microscopy of organic crystals by scanning moiré fringes. *Micron* **120**, 1–9. https://doi.org/10.1016/j.micron.2019.01.014
Schneider NM, Norton MM, Mendel BJ, Grogan JM, Ross FM & Bau HH (2014). Electron–water interactions and implications for liquid cell electron microscopy. *J Phys Chem C* **118**(38), 22373–22382. https://doi.org/10.1021/jp507400n
Schneider CA, Rasband WS & Eliceiri KW (2012). NIH Image to ImageJ: 25 years of image analysis. *Nat Methods* **9**(7), 671–675. https://doi.org/10.1038/nmeth.2089
Sun M, Azumaya CM, Tse E, Bulkley DP, Harrington MB, Gilbert G, Frost A, Southworth D, Verba KA, Cheng Y & Agard DA (2021). Practical considerations for using K3 cameras in CDS mode for high-resolution and high-throughput single particle cryo-EM. *J Struct Biol* **213**(3), 107745. https://doi.org/10.1016/j.jsb.2021.107745
Thust A (2009). High-resolution transmission electron microscopy on an absolute contrast scale. *Phys Rev Lett* **102**(22), 220801. https://doi.org/10.1103/PhysRevLett.102.220801
van den Bergh F (2018). Deferred slanted-edge analysis: A unified approach to spatial frequency response measurement on distorted images and color filter array subsets. *J Opt Soc Am A* **35**(3), 442–451. https://doi.org/10.1364/JOSAA.35.000442
Van Rossum G (2018). *The Python Library Reference, release 3.6.8*.
Van Rossum G & Drake FL (2009). *Python 3 Reference Manual*. pp. 1–242. Scotts Valley, CA: CreateSpace.
Virtanen P, Gommers R, Oliphant TE, Haberland M, Reddy T, Cournapeau D, Burovski E, Peterson P, Weckesser W, Bright J, van der Walt SJ, Brett M, Wilson J, Millman KJ, Mayorov N, Nelson ARJ, Jones E, Kern R, Larson E, Carey CJ, Polat İ, Feng Y, Moore EW, VanderPlas J & SciPy 1.0 Contributors (2020). Scipy 1.0: Fundamental algorithms for scientific computing in Python. *Nat Methods* **17**(3), 261–272. https://doi.org/10.1038/s41592-019-0686-2
Ziatdinov M, Ghosh A, Wong CY & Kalinin SV (2022). AtomAI framework for deep learning analysis of image and spectroscopy data in electron and scanning probe microscopy. *Nat Mach Intell* **4**(12), 1101–1112. https://doi.org/10.1038/s42256-022-00555-8

Appendix

Detector Characterization

Modulation Transfer Function

The frequency response of a detector is characterized by the MTF. That is, the MTF describes how well the spatial

frequencies of an object are transferred to an image or recorded by a detector. The MTF is given by

$$\mathrm{MTF}(f) = |F\{\mathrm{LSF}(x)\}|, \tag{A.1}$$

where f is the spatial frequency, x is the spatial distance, $\mathcal{F}$ denotes the Fourier transform, and LSF(x) is the line spread function (McMullan et al., 2009; Ahmed, 2015; Li et al., 2016).

The LSF is the extension of the point spread function (PSF) from a single point to a line. The PSF characterizes how well an imaging system can resolve two identical points separated by a distance d, by comparing d to their full width at half-maximum (FWHM); if the distance between the two points is equal to or exceeds the FWHM, the detector is capable of resolving the two points. The LSF improves on the PSF by extending the point to a line, thereby sampling a larger number of FWHMs (Ahmed, 2015).

Practically, since creating an ideal line object is difficult, the LSF is obtained by first recording the edge spread function (ESF) and then taking its derivative:

$$\mathrm{LSF}(x) = \frac{d}{dx}[\mathrm{ESF}(x)]. \tag{A.2}$$

To emphasize, the ideal ESF is a step function and so the object required to obtain the ESF is not a one-dimensional thin line, as is required for the LSF; instead, a 2D object is placed just above the illuminated detector to partially block the incoming radiation, thereby generating a sharp transition from detected radiation to undetected radiation, i.e., a step function. However, in a real detector, radiation incident on a pixel will scatter into neighboring pixels, resulting in the blurring of the intensities. In other words, the ESF of a real detector is frequently more akin to a ramp function.

The MTF, therefore, characterizes the blurring or modulation of the intensities associated with the spreading of the radiation into neighboring pixels. The MTF is dependent on ambient conditions, the energy of the incident wavelength, and the physical properties of the detector: the atomic composition of the sensor material and the volume and pitch of the pixels, and the ASIC counting threshold. Furthermore, the MTF is also impacted by the exposure conditions on the detector. At high fluxes, some detectors exhibit nonlinear responses to an input because some of the incident particles are uncounted if they arrive while the detector is processing the impingement of particles that arrived earlier (Fröjdh et al., 2015). Therefore, MTF data must be collected for the exposure conditions used in the experiment in order to accurately simulate images.

Above, it is noted that a 2D object is used to determine the ESF. To improve sampling of the edge and avoid aliasing, the edge object is slanted relative to the x- and y-axes of the detector. This method is dubbed the slanted edge method (Kohm et al., 2003; Masaoka et al., 2014; van den Bergh, 2018). A schematic of the construction of the oversampled ESF is given in Figure A.1. The projected distance from the edge to the center of the pixel, $\mathbf{p}$, is given by X':

$$X' = (\mathbf{p} - s).\mathbf{n}, \quad X' - S = (x,\ y)\frac{(x_n,\ y_n)}{\sqrt{x_n^2 + y_n^2}},$$

since

$$\mathbf{p}.\mathbf{n} = (x,\ y)\frac{(x_\mathbf{n},\ y_\mathbf{n})}{\sqrt{x_\mathbf{n}^2 + y_\mathbf{n}^2}} \text{ and } S = \mathbf{s}.\mathbf{n}, \tag{A.3}$$

where the coordinates of $\mathbf{p}$ and $\mathbf{n}$ are (x, y) and $\frac{(x_n,\ y_n)}{\sqrt{x_n^2 + y_n^2}}$, respectively, and S is a scalar offset that accounts for the choice of the reference point on the edge, $\mathbf{s}$. Equation (A.3) means that the distance between consecutive X'' values is a multiple of $\frac{1}{\sqrt{x_n^2 + y_n^2}}$; that is, the oversampling factor, OF, is

$$\mathrm{OF} = \sqrt{x_\mathrm{n}^2 + y_\mathrm{n}^2}. \tag{A.4}$$

The OF is determined by the angle θ because the values of $x_\mathbf{n}$ and $y_\mathbf{n}$ are determined by the slope of the edge. Subpixel intensities can, therefore, be extracted along the perpendicular normal $\mathbf{n}$ for certain choices of θ. Typically, a predefined number of useful evenly spaced bins is selected, say 4 or 8, which defines the maximum value for OF. The filling of these bins depends on the position of the slanted object relative to the pixel grid, i.e., the edge phase. The edge phase is added to the distance between consecutive X's, and then the number of nonempty bins is inspected. Say, for example, a maximum OF of 4 is desired, the bin spacing is 0.25: giving bins at [0, 0.25, 0.5, and 0.75] along a single pixel. For $\theta = 0.1$ rad, the distance between consecutive X's is ~0.1 pixels, and, in this case, all four bins are filled. For an edge phase equal to 0.3, three bins are filled since the points at which an intensity is extracted are now [0.3, 0.4, 0.5, 0.6, 0.7, 0.8, 0.9, 1, 1.1, and 1.2]. To be clear, each bin has a width equal to 0.25, and so the first bin starting from 0 remains unfilled because no measurement is taken at values in the range [0, 0.25), where [,) denotes a range with an inclusive lower limit and exclusive upper limit. The effective OF is, therefore, given by averaging the number of filled bins for several edge phases. For additional information on the edge phase, see Masaoka (2018).

Detective Quantum Efficiency

The DQE is a quantification of the detector's ability to transfer the energy of an incident particle to the final image signal and is related to the MTF through the equation

$$\mathrm{DQE}(f) = \frac{c^2\mathrm{MTF}(f)^2}{n\mathrm{NPS}(f)}, \tag{A.5}$$

where n is the total number of imaging electrons entering the detector [fluence times specimen area (e)], c is the total counts of the output image, and NPS(f) is the noise power spectrum function (McMullan et al., 2009). The NPS is a measure of how well a detector transfers noise at different spatial frequencies; it is calculated by radially integrating the Fourier transform of an image containing only noise. The DQE is a more useful quantity when evaluating the effectiveness of an imaging system than the MTF alone because it includes the effect of noise on the quality of the output image.

Ideal MTF and DQE

The equations in the Detective Quantum Efficiency section and Modulation Transfer Function section relate to how one would measure the experimental MTF and DQE of a detector; here, consider a perfect ideal pixel. The MTF of a perfect pixel can be found by taking the modulus of the Fourier transform of the LSF of a pixel (Ahmed, 2015), which results in a damped oscillation of the form:

$$\mathrm{MTF}_\mathrm{ideal} = \mathrm{sinc}(f), \tag{A.6}$$

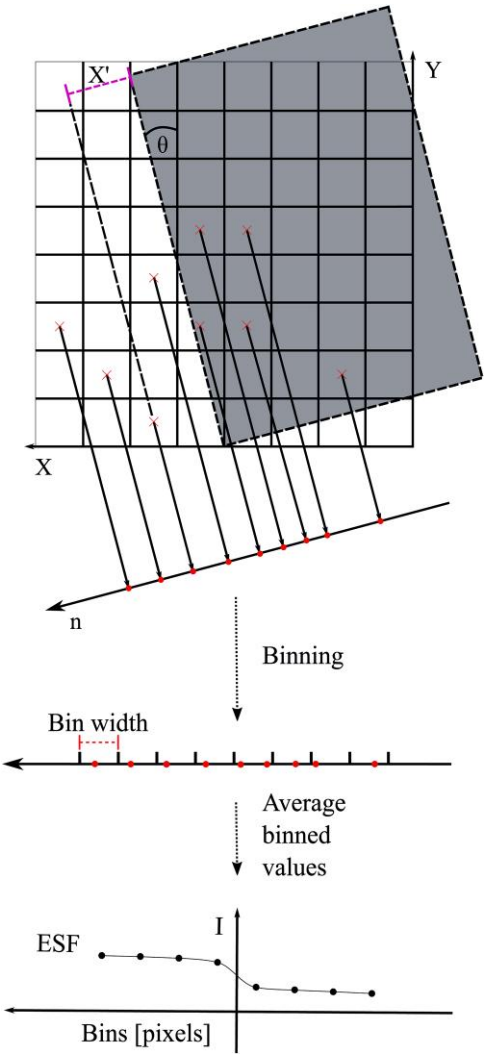

Fig. A.1. Schematic of the oversampled slanted-edge method. The object (gray rectangle with dashed outline) is oriented at an angle θ to the *Y*-axis. The position of each pixel (blood-orange "*x*" marks on the sampling grid) is projected onto the perpendicular normal *n* to obtain the signed distance *X*″. The intensity *I* for every *X*″ value is recorded to form the ESF. The sampling frequency (i.e., the distance between consecutive *X*″s) along n is determined by θ, according to Equation (A.4). Higher sampling frequencies enable extraction of subpixel intensities, resulting in an oversampled ESF. The sampled intensities are binned and averaged to produce the ESF.

where f is the spatial frequency (McMullan et al., 2009). Note, however, for a 2D isotropic homogeneous detector, the MTF is given by

$$\mathrm{MTF}_{\mathrm{ideal\_2D}} = \mathrm{MTF}^2_{\mathrm{ideal}} = \mathrm{sinc}^2(f). \tag{A.7}$$

Contrasting with the MTF, the NPS is a measure of the unwanted noise present in the image. In these simulations, we modeled the discrete nature of electron impingement on the detector with a homogenous Poisson process. The power of the noise for a homogenous Poisson process is constant across all frequencies (Jyoti Bora, 2021); therefore, the characteristic curvature for an ideal homogenous Poisson noise power spectrum is flat and is typically normalized to one.

For a Poisson process, the ideal DQE is defined as

$$\mathrm{DQE} = \frac{\mathrm{MTF}^2}{\mathcal{N}}. \tag{A.8}$$

The symbol $\mathcal{N}$ denotes the normalized power spectrum. The thermal vibrations in a real detector induces a signal at the ASIC, which can reach values just below 5 keV under standard operating temperatures for the Medipix3 (Mir et al., 2017). The impact of the thermal noise on the final image can be minimized by choosing an appropriately high threshold, below which any signal is not recorded. We neglect to include the effects of thermal noise, since the counting thresholds chosen in these simulations is sufficiently high as to eliminate all thermal noise in a real experiment.

Using Equation (A.6) and since $\mathcal{N} = 1$ for all frequencies, the ideal DQE can be defined as

$$\mathrm{DQE}_{\mathrm{ideal}} = \mathrm{sinc}^2(f), \tag{A.9}$$

and

$$\mathrm{DQE}_{\mathrm{ideal\_2D}} = \mathrm{sinc}^4(f). \tag{A.10}$$

Dose, Flux, and Fluence

Dose, flux, and fluence are oftentimes used interchangeably in the literature. Here, we provide an explanation of the intended definition of the terms in the context of this paper. The dose is the absorbed energy per unit mass and has units J/kg. The flux is the number of electrons passing through a surface perpendicular to the electrons' direction per unit time and has units e/Å^{2}s. The fluence is the flux integrated over time and has units e/Å^2. e/pixel is a valid unit of fluence since a pixel has a defined area. The relationship between the fluence and dose is material dependent; the details of their relationship are beyond the scope of this paper. See Schneider et al. (2014) and S'ari et al. (2019) for uses of dose and fluence, respectively, consistent with the work presented here.

Ideal Frequency Response of a Pixel to an Impulse

A single pixel can be modeled as a rectangular function in x and y because it can only measure radiation incident on its rectangular domain. For one dimension, this can be written as

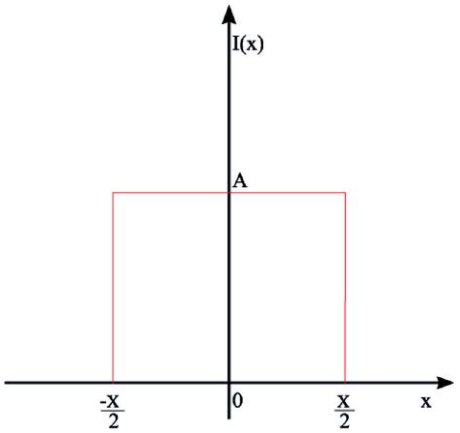

Fig. A.2. Pixel modeled as a rectangular function.

$$I(x) = \begin{cases} A, & -\frac{X}{2} \leq x < \frac{X}{2} \\ 0, & \text{otherwise} \end{cases} \quad \text{(A.11)}$$

where A is the count measured by the pixel within its domain, $-\frac{X}{2} \leq x < \frac{X}{2}$. This is visualized in Figure A.2. The frequency response of the pixel to an impulse with amplitude A is found by taking the Fourier transform of $I(x)$:

$$\text{MTF} = \mathcal{F}[I(x)] = \int_{-\infty}^{+\infty} I(x) e^{-2\pi i f x} dx = \int_{-\frac{X}{2}}^{+\frac{X}{2}} A e^{-2\pi i f x} dx \quad \text{(A.12)}$$

$$= \frac{A}{-2\pi i f}\left[e^{-2\pi i f x}\Big|_{-\frac{X}{2}}^{+\frac{X}{2}}\right] = \frac{A}{-2\pi i f}\left[e^{-\pi i f X} - e^{\pi i f X}\right]$$

$$= \frac{AX}{\pi f X}\left[\frac{e^{\pi i f X} - e^{-\pi i f X}}{2i}\right] = \frac{AX}{\pi f X}\sin(\pi f X) = AX\,\text{sinc}(fX),$$

where $\mathcal{F}$ is the Fourier transform operator and f is the spatial frequency. The final result is obtained using the relation $\text{sinc}(fX) = \frac{\sin(\pi f X)}{\pi f X}$. The same result is obtained in the y direction.

Experimental Comparison Original Trend Lines

Figure A.2 shows the trend lines given by the authors of Mir et al. (2017). Note that the MTF trend lines are compared to the sinc(f) function, where f is the spatial frequency.

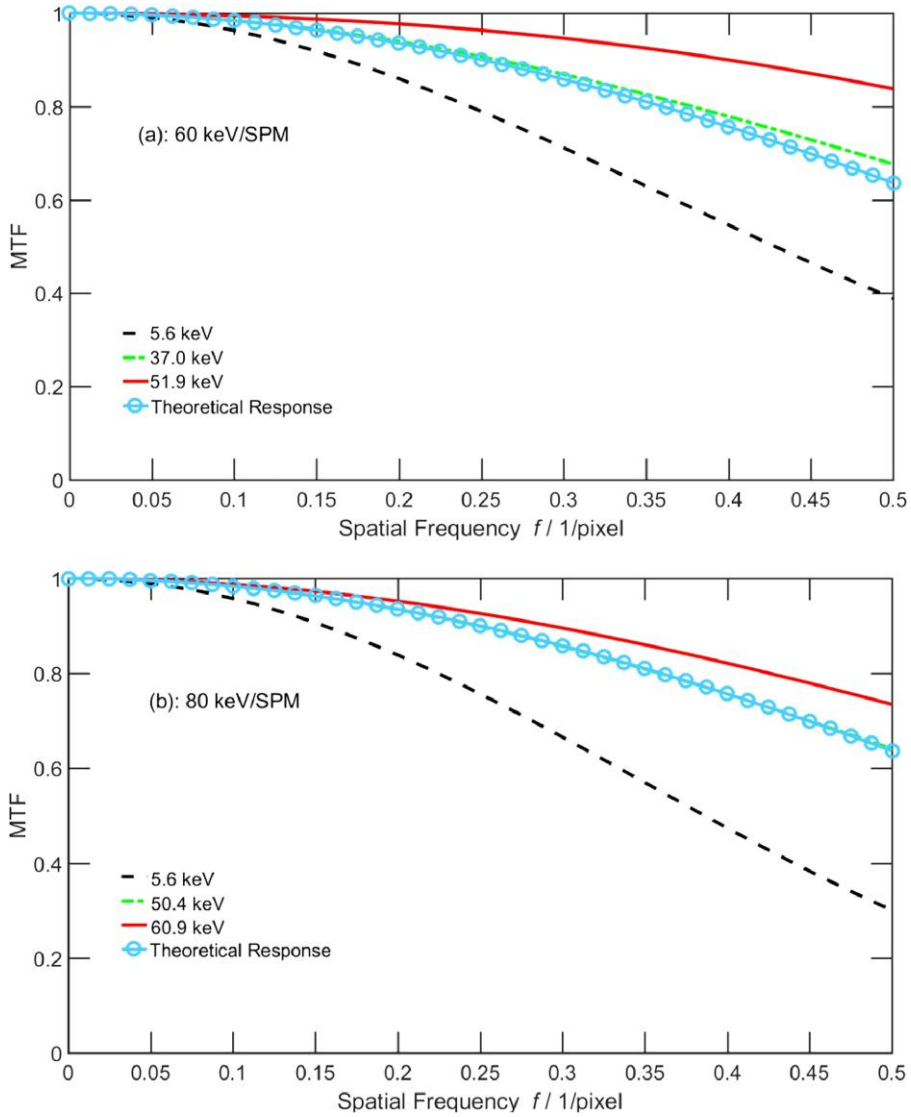

Fig. A.3. Experimental MTF data for the Medipix3 operating in SPM, obtained for 60 and 80 electrons with various values of T_{counting}. We reproduce the figure from Mir et al. (2017) under the Creative Commons CC-BY license.